European Journal of Medicinal Chemistry 287 (2025) 117330

Contents lists available at ScienceDirect

European Journal of Medicinal Chemistry

journal homepage: www.elsevier.com/locate/ejmech

Research paper

Cytotoxic pyrrole-based gold(III) chelates target human topoisomerase II as dual-mode inhibitors and interact with human serum albumin☆

Sheldon Sookai [a,*], Matthew Akerman [b], Mia Færch [c], Yasien Sayed [c], Orde Q. Munro [a,d]

[a] Molecular Sciences Institute, School of Chemistry, University of the Witwatersrand, PO WITS 2050, Johannesburg, South Africa
[b] School of Chemistry, University of KwaZulu-Natal, Pietermaritzburg, 3201, South Africa
[c] Protein Structure-Function Research Unit, School of Molecular and Cell Biology, University of the Witwatersrand, Johannesburg, 2050, South Africa
[d] School of Chemistry, University of Leeds, Woodhouse Lane, LS2 9JT, UK

ARTICLE INFO

Keywords:
Therapeutic
NCI-60
Topoisomerase
Albumin
DNA

ABSTRACT

Topoisomerase IIα (Top II) is a critical enzyme that resolves DNA topology during transcription and replication. Inhibitors of Top II are used as anticancer agents and are classified as interfacial poisons (IFPs) or catalytic inhibitors (CICs). Here, we report a novel class of cytotoxic, stable cationic gold(III) Schiff base chelates (**AuL1**, **AuL2**, and **AuL3**) with DNA-intercalating properties. In the NCI-60 screen, **AuL1** and **AuL3** exhibited potent cytotoxicity (mean GI_{50} values of 11 (7) μM and 14 (9) μM, respectively), whereas **AuL2** showed minimal cytotoxicity. Cluster analysis aligned **AuL1** and **AuL3** with the Top II poison etoposide. Mechanistic studies revealed that **AuL1** acts as an IFP at concentrations between 0.5 and 50 μM and as a CIC at concentrations between 50 and 500 μM. Further investigations demonstrated that all three gold(III) chelates bind to and intercalate DNA, the main substrate for Top II. Finally, binding studies with human serum albumin (HSA) indicated that the chelates have moderate affinity for the protein. Thermodynamic analysis indicates entropically driven binding, with minimal structural disruption observed via UV-CD spectroscopy. These findings highlight the dual mode Top II inhibition mechanism delineated for the gold(III) chelates and their favourable pharmacodynamic interactions with HSA, underscoring their potential as promising anticancer agents.

1. Introduction

The discovery in 1965 that cisplatin [1], a DNA-targeting agent [2,3], inhibits bacterial mitosis, followed by its clinical adoption along with related analogues [4,5] as anticancer metallodrugs [6,7], has catalyzed decades of multidisciplinary research on square-planar platinum(II) complexes [8–11]. However, a significant limitation of most currently available chemotherapeutic agents is their inability to only target cancer cells, leading to severe toxic side effects and drug resistance in cancer cell lines [12–14]. Therefore, the search for new and improved chemotherapeutic agents is of utmost importance. Given that platinum(II) is the only FDA-approved metal ion complex for cancer treatment, and that gold(III) complexes are isoelectronic (d^8) with platinum(II) and form similar square planar tetradentate structures as cisplatin [15], it is a logical choice to investigate novel metal complexes incorporating gold(III) metal ion centres. Despite initial expectations that gold(III) complexes would mimic the biological activity of platinum(II) complexes, their behaviour differs significantly due to their susceptibility to reduction to Au(I) or colloidal gold, Au(0) [16]. This challenge underscores the importance of ligand design in stabilizing the Au(III) oxidation state, ensuring compatibility with standard solutions and physiological media [17,18].

Multidentate ligand frameworks commonly used to stabilize the Au(III) ion include CNC-type pincer ligands [19–22], porphyrins [23], and deprotonated pyrroles [24]. These ligands are characterized by strong σ-donor atoms (C, N, and O), either neutral or anionic, which align well with the hard Lewis acid properties of the Au(III) ion. By donating electron density to the metal centre, these ligands reduce the metal's susceptibility to reduction, thereby enhancing its stability [25]. Pyrrole-based ligands serve as critical components in a range of organic pharmaceuticals [26], exemplified by clinically approved drugs such as Tolmetin [27]; Glimepiride [28]; and Sunitinib, [29]. Notably,

---

☆ Electronic Supplementary Information (ESI) available: Complete experimental details and supplementary tables and figures in PDF format, X-ray crystal structures in CIF format (CCDC 2408008, 2408009 and 2408010).

* Corresponding author.
E-mail address: Sheldon.Sookai@wits.ac.za (S. Sookai).

https://doi.org/10.1016/j.ejmech.2025.117330
Received 23 December 2024; Received in revised form 24 January 2025; Accepted 24 January 2025

pyrrole-imine metal chelates hold considerable medicinal promise. Among these, the pentadentate macrocycle texaphyrin [30] is particularly well-known for its ability to chelate Lu(III) [31], showing potential as a candidate for photodynamic therapy, although it is not yet FDA-approved [32].

In biological systems, the ability of metal complexes to target specific “druggable” macromolecules such as DNA and enzymes has significant implications for therapeutic applications. Of relevance to this study, few gold(III) complexes have been reported to specifically target topoisomerase II (Top II). Top II is an ATP-dependent nuclear enzyme requiring Mg^{2+} ions to modulate DNA topology [33,34], and is critical for replication and transcription [35–37]. It functions by transiently creating and resealing double-stranded DNA breaks, mediated by active-site tyrosine residues, forming cleavage complexes (Top II cc) to maintain genome stability [38–41]. Dysregulation of Top II leads to an accumulation of Top II cc, disrupting DNA processes and triggering apoptosis [38–41]. Top II inhibitors are categorized into poisons and catalytic inhibitor compounds (CICs) [38]. Poisons irreversibly trap the DNA-enzyme complex, with interfacial poisons (IFPs) binding non-covalently to distort the active site and covalent poisons enhancing cleavage by blocking the enzyme’s N-terminal gate. CICs, in contrast, inhibit Top II enzymatic activity without inducing DNA breaks [38, 42–44], disrupting steps such as DNA binding [38,39,45] and ATP hydrolysis, offering reduced toxicity and safer therapeutic potential compared to poisons.

Understanding the binding of chemotherapeutic agents to human serum albumin (HSA) is critical for optimizing drug distribution and efficacy *in vivo* [46]. HSA, the most abundant plasma protein (600 μM) [47], plays a key role in maintaining osmotic pressure and transporting both endogenous and exogenous molecules [48]. Structurally (Scheme 1), HSA is a heart-shaped macromolecule comprising 585 amino acids, with a monomeric mass of 66.5 kDa [49]. It is organized into three domains (I, II, and III), each with two subdomains (A and B) [49,50]. The protein contains multiple binding sites, primarily for fatty acids, as well as two main small molecule binding sites: Sudlow’s sites I (in subdomain IIA) and II (in subdomain IIIA) [51–53]. These sites are critical for the pharmacokinetics and pharmacodynamics of drug candidates, as HSA’s binding affinity can significantly influence drug distribution and efficacy *in vivo* [51].

In this study, we synthesized three bis(pyrrole-imine) Schiff base Au(III) chelates, specifically **AuL1**, **AuL2**, and **AuL3** (Scheme 1), and investigated their binding to HSA using spectroscopic methods in KH_2PO_4 (50 mM, pH 7.5). Our goal was to determine how the structural variations in the carbon chain linking the imine groups influence chelate uptake by HSA and to identify their preferred binding site(s). Additionally, we screened the three compounds in the NCI-60 panel of human cancer cell lines to evaluate their cytotoxicity. Notably, **AuL1** and **AuL3** showed sufficient activity for further evaluation in a five-dose screen, while **AuL2** exhibited no significant cytotoxicity. Our results suggest that **AuL1** exerts its cytotoxic effect by intercalating DNA and inhibiting Top II activity, acting as both an interfacial poison (IFP) and a catalytic inhibitor compound (CIC).

2. Results and discussion

2.1. Ligand synthesis

Ligands **H_2L1–H_2L3** were metalated with Au(III) by reacting with $[Bu_4N][AuCl_4]$ (Scheme 1), yielding the corresponding Au(III) chelates **AuL1**, **AuL2**, and **AuL3**. These compounds represent an extension of our patented class of cytotoxic molecules [54]. Specifically, we utilized pyrrole-imine Schiff base chelates, selected for their capacity to stabilize the Au(III) ion in its high oxidation state. During metalation, the nitrogen atoms of the pyrrole rings are deprotonated [55], resulting in the formation of the desired cationic chelates. The desired gold(III) chelates were obtained as pure precipitates directly from the reaction mixture (Figs. S1–33).

2.2. X-ray structures

The solid-state structures of the three gold(III) chelates were elucidated by single-crystal X-ray diffraction (Fig. 1). **AuL1** crystallized in the triclinic space group P-1, while **AuL2** and **AuL3** crystallized in the monoclinic space groups $P2_1/n$ and $P2_1/c$, respectively. Each complex exhibited the expected four-coordinate, square planar geometry, consistent with their tetradentate bis(pyrrolide-imine) chelate design ideal for potential DNA binding and cytotoxic activity [57]. The Au–N bond lengths in **AuL1**, **AuL2**, and **AuL3** ranged from 1.999(2) to 2.012 (17) Å, with average distances of 2.011(11) Å for Au–N_{imine} and 2.001 (11) Å for Au–$N_{pyrrole}$ (0.48 % shorter). This reflects the enhanced σ-donor nature of the deprotonated pyrrole moiety with more acute C–N–C angles than the corresponding C═N–C angles of the imine donors.

The coordination group bond distances are comparable to those

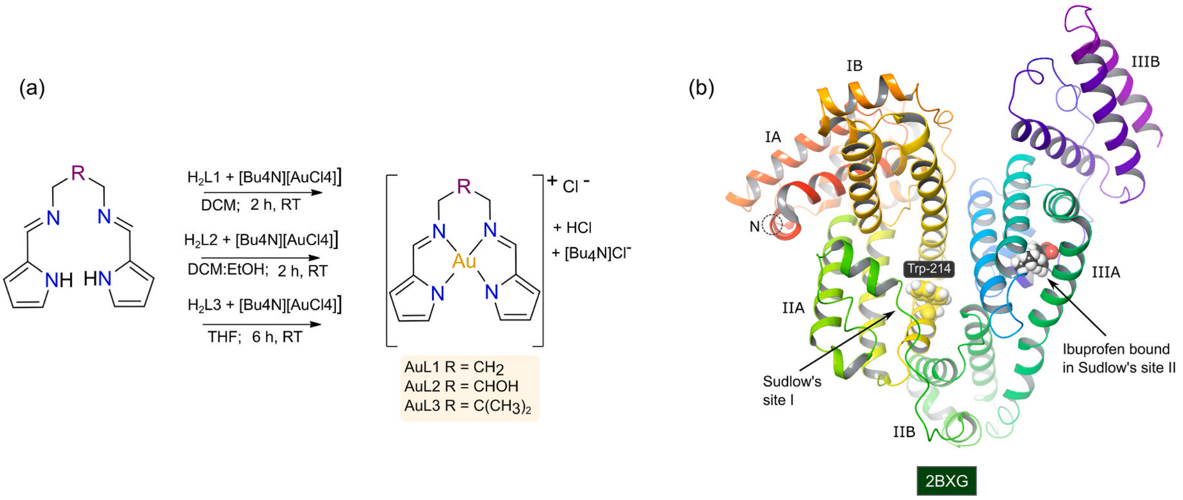

Scheme 1. (a) Synthetic protocol for producing **AuL1**, **AuL2**, and **AuL3** by reaction of the appropriate bis (pyrrolide–imine) ligands with $[Bu_4N][AuCl_4]$. (b) X-ray structure of HSA bound to indomethacin (redrawn from PDB code 2BXH) [56], illustrating the two primary small molecule binding sites. Sudlow’s site I is larger than Sudlow’s site II, and compounds that bind in this pocket perturb the fluorescence of Trp-214. The protein secondary structure elements are depicted schematically, coloured by domain, and labelled.

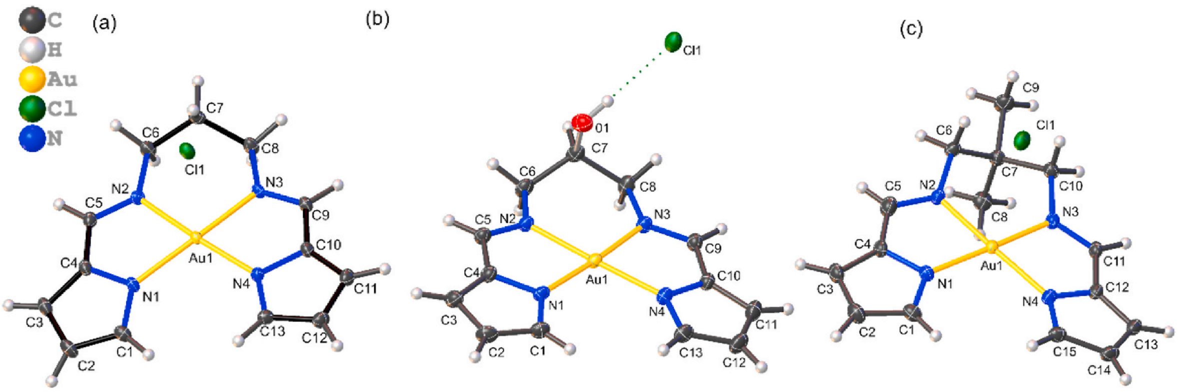

Fig. 1. Perspective views of the asymmetric units of the bis(pyrrolide-imine) Au(III) chelates (a) **AuL1**, (b) **AuL2**, and (c) **AuL3**. The cationic complexes are shown with their respective chloride counterions (50 % thermal ellipsoids for all non-H atoms; H atoms are rendered with arbitrary radii). Crystallographic details are presented in the Supporting Information.

reported in similar gold(III) complexes in the range of 1.928–2.216 Å [57,58]. However, the average $N_{pyrrole}$–Au–$N_{pyrrole}$ and N_{imine}–Au–N_{imine} bond angles for the gold(III) chelates are 102.5(8)° and 95.4 (7)°, respectively, which marginally deviates from the structurally-related gold(III) complex analogues $N_{pyrrole}$–Au–$N_{pyrrole}$ and N_{imine}–Au–N_{imine} bond angles, that are 98.83(4)° and 97.6(4)°, respectively [57]. This is a consequence of the ligand bite. Notably, the cation conformations deviate slightly from planarity due to non-bonded crystal packing forces and discrete π-stacked dimer formation. Despite the π-stacking, no aurophilic Au⋯Au contacts were observed (Au⋯Au distances >4 Å), suggesting an alternative stabilization mechanism that could be relevant for DNA/drug conjugate formation. Key bond parameters are summarized in Table 1. Further analysis of the gold(III) chelates is presented in the ESI (Figs. S34–36).

2.3. Stability of AuL1 in blood plasma

The stability of a metallodrug candidate is critical for several reasons, including its ability to retain its ligand(s) when interacting with biomolecules and to remain intact in the bloodstream long enough to reach its intended target site(s). Several metallodrug candidates, such as NAMI-A, cisplatin and auranofin, often undergo ligand exchange reactions, ultimately interacting with biomolecules as simpler ionic metal species [59,60]. In contrast, the gold(III) complex **AuL1** demonstrated remarkable stability over prolonged periods in human plasma (Fig. 2). No chemical changes of the gold(III) complex such as bond dissociation or metal ion release could be detected over 24 h. The stability of **AuL1** in human plasma was evaluated *in vitro* as a function of time using UV–visible spectroscopy (Fig. 2). The spectral kinetic data reveal partial precipitation of the complex within the first 6 h, which is earmarked by the lack of isosbestic points accompanying the spectral changes. By 22 h, the decrease in absorbance accompanied by band broadening is attributed to both complex precipitation as well as an increase in the turbidity of the human plasma solution. Importantly, the spectral band maximum throughout the 24 h time period only changes in intensity and does not undergo wavelength shifts. This indicates the absence of chemical reactions such as complex hydrolysis or demetallation.

Table 1
Selected bond lengths and bond angles for **AuL1**, **AuL2** and **AuL3**.

Bond distances Å	AuL1	AuL2	AuL3
Au–$N_{pyrrole}$	2.002(17)	1.999(2)	2.002(14)
Au–N_{imine}	2.012(17)	2.012(2)	2.008(14)
C–C=N	1.300(3)	1.305(3)	1.304(2)
Bond angles (°)			
$N_{pyrrole}$–Au–$N_{pyrrole}$	102.4 (7)	102.4(9)	102.7(7)
Cis–$N_{pyrrole}$–Au–N_{imine}	80.94(7)	80.79(9)	81.15(6)
Trans–$N_{pyrrole}$–Au–N_{imine}	175.91 (7)	176.5(9)	174.1(6)
N_{imine}–Au–N_{imine}	95.95(7)	95.61(9)	94.53(6)
$C_{pyrrole}$–C–N_{imine}	117.3(19)	117.2(2)	117.5(16)

[a] The full list of bond lengths and bond angles is reported in the ESI (Tables S2–S11).

2.4. NCI-60 cytotoxicity screens

All three gold(III) chelates were accepted for initial single-dose NCI-60 cytotoxicity screens (10 μM test agent concentration) by the National Cancer Institute (NCI, Bethesda, MD) against a panel of 60 human cancer cell lines (Figs. S37–S39). Of the three compounds screened, only **AuL1** and **AuL3** were sufficiently cytotoxic in phase 1 (the single-dose assay) to warrant the full five-dose NCI screen (phase 2) spanning the concentration range 1×10^{-9} to 1×10^{-5} M (Table 2). Full cytotoxicity data over the NCI's panel of 60 human cancer cell lines is presented in the ESI.

From the one-dose screens, the mean growth percentages were 78, 98, and 92 % for compounds **AuL1**–**AuL3**, respectively. From the five-dose screen of **AuL1** and **AuL3**, the lowest IC_{50} values were for the ovarian cancer cell lines OVCAR-3 (4.0 μM) and IGROV1 (9.8 μM) and the colon cancer cell line SW- 620 (15 μM). Fig. 3 compares the best GI_{50} values for compounds **AuL1** and **AuL3** with corresponding data from clinically deployed anticancer drugs with established MOAs. The average cytotoxicity parameters for **AuL1** and **AuL3** obtained for each of the nine classes of human cancer in the NCI-60 screen are summarized in Table 2. Collectively, the data indicate that colon and ovarian cancer cell lines are, on average, the most susceptible to the gold(III) complex with several cell lines exhibiting GI_{50} and IC_{50} values below 10 and 20 μM, respectively (Figs. S37 and S39).

Several noteworthy points emerge from the comparative data of Fig. 2: (i) **AuL1** and **AuL3** have similar cytotoxicity against LC–NCI–H522, with **AuL1** overall being more cytotoxic in all cell lines apart from LE-HL-60, LE-RMPI-8226 and CO-HCT-15. (ii) The cytotoxicity of both gold(III) chelates compares favourably with that of etoposide and against some cell lines they are more potent cisplatin (Figs. S40 and 41). (iii) Taxol and Daunorubicin are the most potent anticancer drugs with nanomolar GI_{50} values. The growth inhibition data for both **AuL1** and **AuL3**, both on average and for the most sensitive cancer cell lines (CO-HCT-15 and LE:HL-60 for **AuL1** and **AuL3**, respectively), therefore do not compare favourably with the potent cytotoxicity exhibited by Taxol and Daunorubicin. It should be noted that a successful anticancer compound is not necessarily reliant on sub micromolar GI_{50} values. A typical example is 5-fluoruracil, which has a GI_{50} value that exceeds 10 μM for most cancer cell lines, however, the drug is still widely administrated as an antineoplastic antimetabolite [62,63].

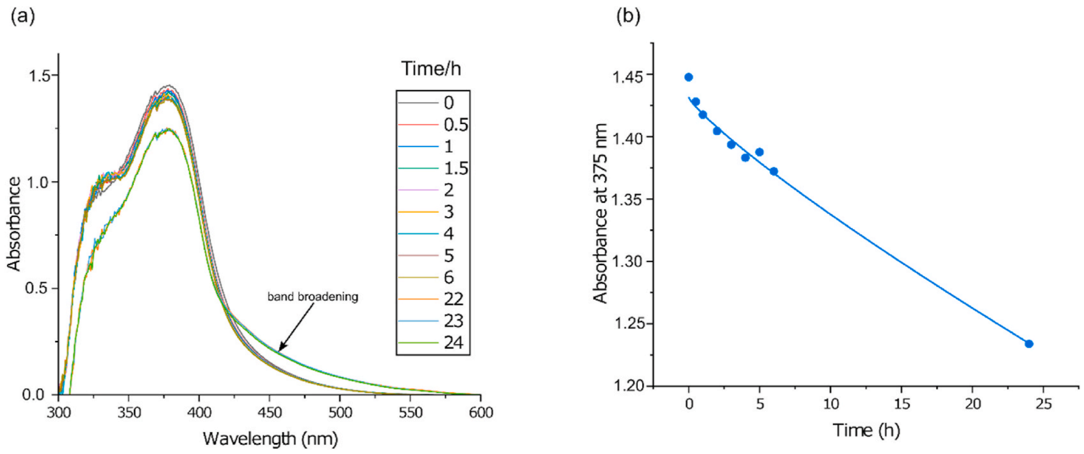

Fig. 2. Stability of **AuL1** measured in human plasma. (a) UV–visible spectral changes for **AuL1** (100 μM) recorded in a solution of human plasma diluted with phosphate buffer (50 mM KH_2PO_4, pH 7.50, 1:4 ratio) as a function of time. (b) Nonlinear least-squares regression fit of the absorbance decay curve to a single exponential function.

Table 2
Summary of cytotoxicity parameters for **AuL1** and **AuL3** from a five-dose screen against the NCI's panel of 60 human cancer cell Lines[a].

	AuL1				AuL3			
Cancer	N[b]	GI_{50}	IC_{50}	LC_{50}	N[b]	GI_{50}	IC_{50}	LC_{50}
Leukaemia	6	3.46 (2)	15 (10)	>100	6	3.6 (1)	36 (27)	>100
Non-small cell lung cancer	9	16 (10)	40 (30)	64 (30)	9	27 (23)	37 (17)	80 (31)
Colon cancer	7	8.38 (7)	18 (12)	40 (22)	7	13 (11)	43 (33)	68 (33)
CNS cancer	6	13 (5)	27 (8)	58 (15)	6	12 (7)	30 (11)	7 (24)
Melanoma	8	10 (4)	23 (5)	50 (6)	8	14 (5)	31 (4)	68 (14)
Ovarian cancer	6	18 (15)	37 (30)	60 (20)	6	17 (5)	34 (8)	72 (15)
Renal cancer	8	6.5 (9)	24 (31)	44 (25)	8	13 (7)	33 (9)	68 (19)
Prostate cancer	2	12 (3)	26 (6)	52 (12)	2	16 (3)	41 (0.1)	95 (7)
Breast cancer	8	7.9 (6)	21 (8)	51 (9)	8	2 (16)	41 (30)	66 (3)
Average	60	11 (7)	26 (16)	58 (27)	60	14 (9)	36 (14)	66 18)

[a] Abbreviations: N, number of cell lines within each cancer category; GI_{50}, compound concentration effecting 50 % growth inhibition; IC_{50}, compound concentration effecting 100 % growth inhibition; LC_{50}, compound concentration that induces 50 % cell death.

[b] Total number of cell lines used. Estimated standard deviations are given in parentheses; large values indicate variable susceptibility of a specific group of cell lines to the test compound.

The mean IC_{50} values (0 % cell growth rate) across all 60 cancer cell lines for **AuL1** and **AuL3** were determined to be 26(16) μM and 36(14) μM, respectively. This variance reflects differences in the cytotoxicity of the gold(III) chelates across various groups of cancer cell lines. A comparison of the best GI_{50} (50 % cell growth rate) values for **AuL1** and **AuL3** with those of clinically approved anticancer drugs is presented in Fig. 4a, revealing that while their GI_{50} values were higher than those of some commercial drugs, the LC_{50} (−50 % growth rate) and IC_{50} values of **AuL1** and **AuL3** were lower than those of cisplatin and mitomycin, which have broad and rather shallow dose-response functions. The cytotoxicity profile of **AuL1** was comparable to the chiral Au(III) chelate **[Au(1S,2S-L7)] PF$_6$**. Notably, the IC50 values were comparable to those of mitomycin, a well-known anticancer agent. This difference highlights the unique behaviour of the synthesized compounds.

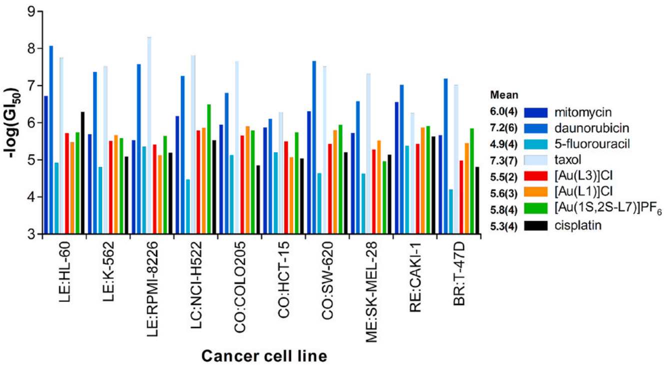

Fig. 3. Selected NCI cytotoxicity data for **AuL1** and **AuL3**, our previously reported cytotoxic complex **[Au(1S,2S-L7)] PF$_6$** [61], and clinically employed anticancer drugs with known MOAs. The bar chart plots the concentrations at which 50 % growth inhibition occurs (GI_{50}) against the human cancer cell line for the indicated compounds. Tall bars correspond to more active growth inhibition by the test agents. Abbreviations: LE, leukaemia; LC, non-small lung cancer; CO, colon cancer; CNS, central nervous system cancer; ME, melanoma; OV, ovarian cancer; RE, renal cancer; PR, prostate cancer; BR, breast cancer.

The gold(III) chelates exhibited significantly steeper dose-response curves compared to the commercial drugs. This steepness indicates that while higher concentrations are initially required to reach the cytotoxicity threshold, small increases beyond this point result in a sharp rise in cell mortality. Such dose-response behaviour suggests a potentially more selective mechanism of action, which could reduce the risk of sublethal dosing and the likelihood of resistance development. These findings underscore the potential of **AuL1** and **AuL3** as promising candidates for further investigation.

A key question is whether the GI_{50}, IC_{50}, and LC_{50} values obtained from the NCI-60 5-dose screen for a compound with an unknown MOA can be statistically analysed to predict a likely MOA or cellular target. To do this we have used hierarchical cluster analysis (Fig. 4b) using the set of GI_{50}, IC_{50}, and LC_{50} values for **AuL1**, **AuL3** and 21 reference compounds with well-characterized MOAs to determine a likely target for **AuL1** and **AuL3** *in vivo*. The analysis revealed that **AuL1** has a direct link with etoposide (a widely used Top II poison), suggesting **AuL1** may have a similar MOA to etoposide [64]. Additionally, **AuL1** showed a more distant relationship with daunorubicin, a potent Top II poison, and cisplatin, which acts as both a Top II inhibitor and DNA cross-linker [65]. This clustering pattern indicates that **AuL1** may interact with DNA in a manner akin to these reference drugs, likely involving Top II

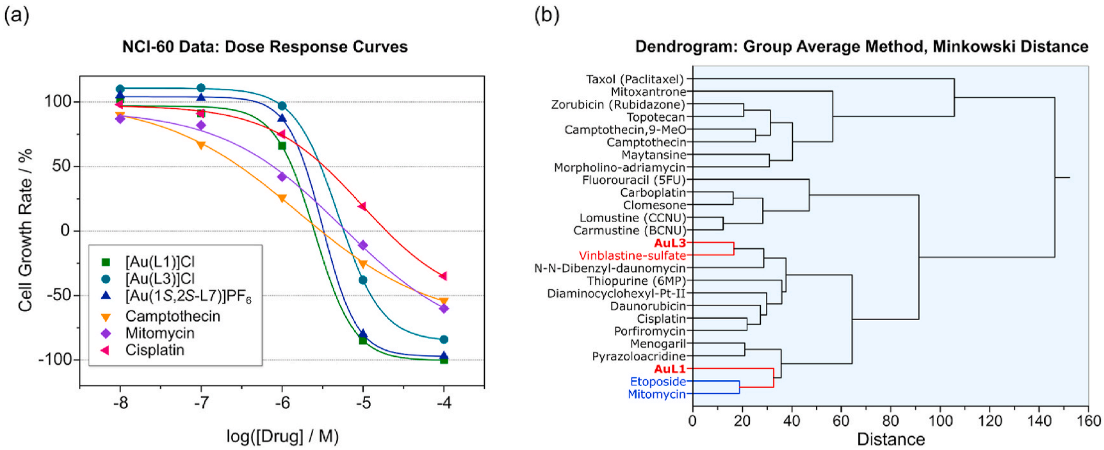

Fig. 4. (a) Dose-response curves for the colon cancer cell line COLO-205 treated three commercial anti-cancer agents (camptothecin, cisplatin, and mitomycin) and the two Au(III) chelates that were selected for the NCI-60 five-dose screen (**AuL1** and **AuL3**) along with the previously reported chiral Au(III) complex **[Au(1*S*,2*S*-L7)] PF$_6$**. (b) Hierarchical cluster analysis comparison of the NCI-60 cytotoxicity profiles of clinically deployed drugs with known modes of action and the Au(III) chelates **AuL1** and **AuL3** synthesized here. The NCI-60 data were collated from the DTP drug repository database.

inhibition. Based on this analysis, it is hypothesized that both **AuL1** and **AuL3** share a similar DNA binding mode. This is consistent with the UV-LD and CD spectroscopy data, which suggested intercalative binding and a significant impact on DNA conformation (*vide infra*). To validate the MOA proposed for **AuL1** and **AuL3** based on hierarchical cluster analysis, initial *in vitro* enzyme inhibition assays targeting Top II and Top I are necessary. Given that topoisomerase inhibitors are classified as IFPs (interfacial poisons) or CICs (catalytic inhibitor compounds), it is crucial to employ experimental methods capable of differentiating between these two MOAs.

2.5. Topoisomerase IIα inhibition assay

Because both gold(III) complexes statistically resemble the NCI-60 cytotoxicity profile of etoposide, which specifically targets Top II, we have used a Top IIα enzyme inhibition assay (TopoGEN) to delineate the dose response function for **AuL1** with the enzyme. The agarose gel image in Fig. 5a demonstrates that **AuL1** concentrations below 500 nM resulted in undetectable levels of linear DNA cleavage product, indicating no trapping of the Top II-DNA cleavage complex. In contrast, concentrations of **AuL1** between 0.5 and 50 μM (lanes 5–7) showed a nonlinear increase in the amount of linear DNA as a function of [**AuL1**] concentration. The dose-response curve peaked at [**AuL1**] = 5 μM, after which a nonlinear decrease was observed at higher concentrations (50–500 μM, lanes 7 and 8) Fig. 5b.

The overall dose-response function is therefore a normal biphasic with a skewed bell-like shape. The bell-shaped dependence of the linear DNA product concentration upon increasing [**AuL1**] is well-fitted to a Gaussian response function (GaussAMP). In effect, there are two clear opposing dose-response functions. The first binding event is a positive binding dose-response, and its midpoint is marked by A on the graph with a $K_{a1} = 7.46 \times 10^{-6}$ M^{-1} and $n \sim 2$. The stoichiometry of 2 is consistent with two binding sites for **AuL1** in the first equilibrium [66]. The negative dose response (i.e., the second binding event), has a midpoint marked B on the graph, $K_{a2} = 181 \times 10^{-6}$ M^{-1}, and $n \sim 1$. The stoichiometry indicates a single binding site for **AuL1** in the second equilibrium. The biphasic dose-response function, dual equilibrium association constants, and the stoichiometry above clearly indicate a switch in the reaction mechanism from compound **AuL1** initially behaving as an IFP (0.5–50 μM^{-1}) capable of trapping the DNA-Top II covalent cleavage complex to the gold(III) chelate then operating as a CIC (50–500 μM^{-1}) in which the enzyme is sterically blocked from binding to its DNA substrate.

Mechanistically, the first phase can be attributed to the non-covalent binding of two molecules of **AuL1** to the Top II-DNA intermediate covalent cleavage complex (Top IIcc) at its two nick sites. This binding mechanism closely resembles that observed in the X-ray structure of the quaternary-(drug)$_2$-DNA enzyme covalent cleavage complex of VP-16 (etoposide; PDB 5GWK) [45]. As depicted in Fig. 5a, an increase in the fraction of **AuL1** from 0.5 to 5 μM leads to an increase in the trapped (i.e., poisoned) fraction of the DNA-enzyme intermediate covalent Top II cc during the catalytic cycle of the enzyme. This accounts for the increase in the amount of linear DNA product isolated from the reaction. At higher concentrations of **AuL1** (50–500 μM), a mechanistic switch in action occurs, wherein **AuL1** exhibits an additional target with a lower binding affinity (K_{a2}) compared to its insertion at the Top II cc nick sites (K_{a1}). This phenomenon is evident in Fig. 5a, where the formation of supercoiled DNA (SC) in lanes 7 and 8 indicates the inability of the binary DNA-enzyme complex to form due to the binding of the drug to the protein.

Consequently, **AuL1** catalytically inhibits the enzyme at these higher concentrations. As discussed later (Fig. 8a), **AuL1** binds to and intercalates with DNA (with a K_a of 1.95 x 10^4 M^{-1}), predominantly at the AT sites of the DNA sequence [67]. It is conceivable that the binding of **AuL1** to the DNA sequence targets the same sites as Top II. Therefore, as the concentration of **AuL1** increases, it competes with the nick site-binding and ultimately outcompetes Top II in binding to DNA. At high concentrations of **AuL1**, the dominant mechanism of Top II inhibition becomes unconventional catalytic inhibition (drug binds to the substrate) rather than enzyme poisoning. This is evidenced by the inverse relationship between the intensity of the linear DNA band and [**AuL1**] when [**AuL1**] exceeds 5 μM (lanes 7 and 8, Fig. 5a). Strikingly, the K_a delineated from the Top II inhibition curve (K_{a2}) is within 1σ of the K_a for **AuL1** binding to ctDNA (181 μM ≈ 195 ± 0.1 μM, see below).

Based on previous studies on the catalytic mechanism of Top II [68] and the enzyme poisoned by etoposide [45], we have developed a simplified mechanistic scheme (Fig. 6) that effectively summarizes the current data. The catalytic inhibition of Top II by **AuL1** exhibits similarities to a dual-mode irreversible DNA-enzyme covalent complex trapper (IFP) catalytic inhibitor, as reported in previous studies for anti-cancer agents such as 9-hydroxyellipticine [68], adriamycin (doxorubicin) [69,70], and *cis*-dichloro{(isoquinolin-3-ylcarbonyl)[2-[(isoquinolin-3-ylcarbonyl)amino]phenyl]azanido} Au(III) [66]. In summary, our findings indicate that the dual-mode reaction of **AuL1** with Top II is consistent with earlier observations for similar biphasic inhibition of the enzyme observed with other anti-cancer therapeutics. The enzyme inhibition data obtained in our study further support the MOA of **AuL1**, as identified from the *in vitro* cytotoxicity data (GI$_{50}$

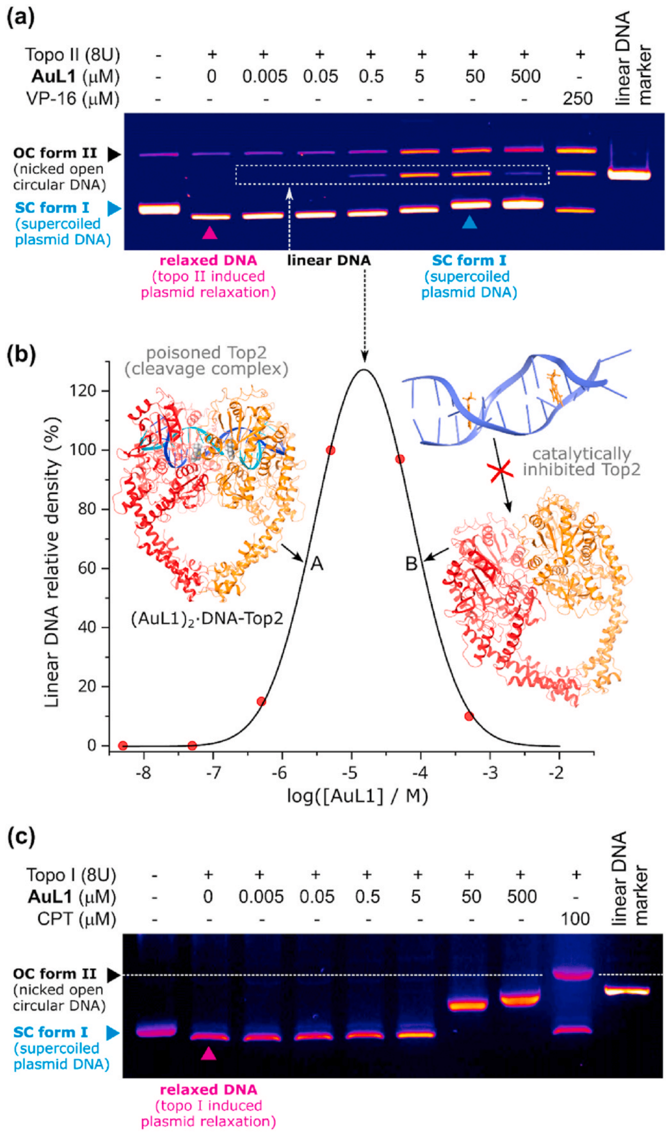

Fig. 5. (a) Electrophoretic analysis (1 % agarose gel, 0.5 μg mL^{-1}, EB) of a topoisomerase II (Top II) plasmid DNA relaxation assay (negatively supercoiled pHOT1 plasmid DNA; TopoGEN, Inc, 30 ng $well^{-1}$) as the substrate, an enzyme concentration of 8 units (U), etoposide (VP-16) as the Top II poison control (250 μM), and compound **AuL1** as the test agent over a concentration range of 0.005–500 μM. All annotated lanes, unless otherwise indicated, contain Top II. (b) The gaussian response curve reflects a nonlinear fit of the linear DNA peak relative intensity (proportional to the concentration) as a function of compound dose for the highlighted linear DNA bands. (c) Electrophoretic analysis of topoisomerase IB (Top1) cleavage assay employing SC plasmid DNA (pHOT1, 188 ng μL^{-1}) as the substrate, an enzyme concentration of 8 U μL^{-1} (in all annotated lanes except the first), CPT (100 μM) as the Top1 poison control, and compound **AuL1** over a concentration range of 0.005–500 μM. The gel (1 % agarose) contains EB (0.5 μg mL^{-1}).

values) through hierarchical cluster analysis.

2.6. Topoisomerase I inhibition assay

To validate that **AuL1** specifically inhibits Top II and confirm the accuracy of our hierarchical cluster analysis, a second set of experiments was conducted to assess its ability to inhibit or poison topoisomerase I (Top1). Top1 differs from Top II because it induces single-strand breaks instead of double-strand breaks during the DNA relaxation reaction. The results of the Top1 activity assay are presented in the agarose gel (Fig. 5c). Camptothecin (CPT), a potent Top1 poison, was used as a reference. CPT traps (via intercalation) the Top1-DNA covalent cleavage complex intermediate in the catalytic cycle. Because a single strand of the DNA substrate is nicked in the trapped covalent cleavage complex, this leads to a significant concentration of nicked open circular DNA in the reaction mixture after work-up. Our gel assay data indicate that concentrations of [**AuL1**] ranging from 0.005 to 500 μM were completely ineffective in poisoning Top1 because no nicked open circular DNA is formed over the entire dose range. Notably, for 0.005–5 μM doses of **AuL1**, Top1 clearly efficiently relaxes pHOT1 DNA since no supercoiled DNA is present in lanes 2–6. This confirms the complete lack of interaction of **AuL1** with Top1 and/or its DNA substrate at these doses. In lanes 7 and 8 (50 and 500 μM **AuL1**), marked band shifts are observed (to lower Rf values) for the supercoiled plasmid substrate in unison with brighter imaging by EB (intercalator dye). This suggests that at high enough doses of **AuL1**, DNA binding via intercalation occurs, leading to localized changes in the degree of winding of the supercoiled substrate, thereby enhancing its affinity for the dye and substantially changing its mobility. It can thus be concluded that the Au(III) chelates synthesized in this study demonstrated specific targeting of Top II, highlighting their potential for further exploration as anti-cancer therapeutics.

2.7. AuL2 is not as potent as AuL1 and AuL3 in the NCI-60 screen

In contrast to both **AuL1** and **AuL3**, **AuL2** exhibited significantly lower cytotoxicity in the NCI-60 screen. Therefore, **AuL2** activity against Top II was investigated using the Top II inhibition assay (Fig. 7a). Interestingly, **AuL2** has a comparable level of activity to **AuL1** in the assay. Specifically, the compound poisons Top II at low concentrations (0.5 μM) and competitively inhibits the enzyme at high concentrations (50 μM). These results closely resemble those of **AuL1**, indicating that **AuL2** is a potent poison of topoisomerase II *in vitro* and acts as an enzyme inhibitor at higher concentrations.

This difference in NCI-60 cytotoxicity of **AuL2** *in vitro* may be attributed to the presence of an OH group at the second position of the alkyl linking group on the molecule. We propose two potential explanations for the lower cytotoxicity and inactivity observed for **AuL2**: (i) Efflux Pump Elimination; **AuL2** may be more susceptible to elimination via efflux transporters, such as P-glycoprotein (P-gp) or multidrug resistance protein 1 (MRP1), which are well-known mechanisms responsible for reducing the intracellular concentration of toxic compounds. Structural features of **AuL2**, including the OH moiety, may enhance recognition by these transporters, leading to rapid clearance from cancer cells [71]. (ii) Increased Serum Protein Binding; The OH group in **AuL2** may also enhance its binding affinity to serum proteins, particularly HSA, facilitating its transport and elimination from the bloodstream (*vide supra*). This increased binding could limit the amount of free, active compound available for cellular uptake, thereby reducing its cytotoxicity.

It is worth noting that, although **AuL2** was not sufficiently cytotoxic to progress to the NCI-60 phase two screening, it demonstrated significant potency against several cancer cell lines at a concentration of 10 μM. These include non-small cell lung cancer NCI–H522 (14.62 % growth), colon cancer SW-620 (51.35 % growth), and breast cancer MDA-MB-468 (58.56 % growth), as well as partial cytotoxicity toward leukaemia cell lines (Fig. S38).

2.8. The gold(III) ion is essential for cytotoxicity

Additional experiments were conducted to further support the hypothesis that the cytotoxicity of the chelates is primarily attributed to the Au(III) ion. These experiments replicated the gel electrophoresis tests performed on **AuL1**, but this time the Top II enzyme was incubated with supercoiled DNA and varying concentrations of the Pd(II) analogue of **AuL1**, as well as **H_2L1**, in separate experiments (Fig. 7b and c).

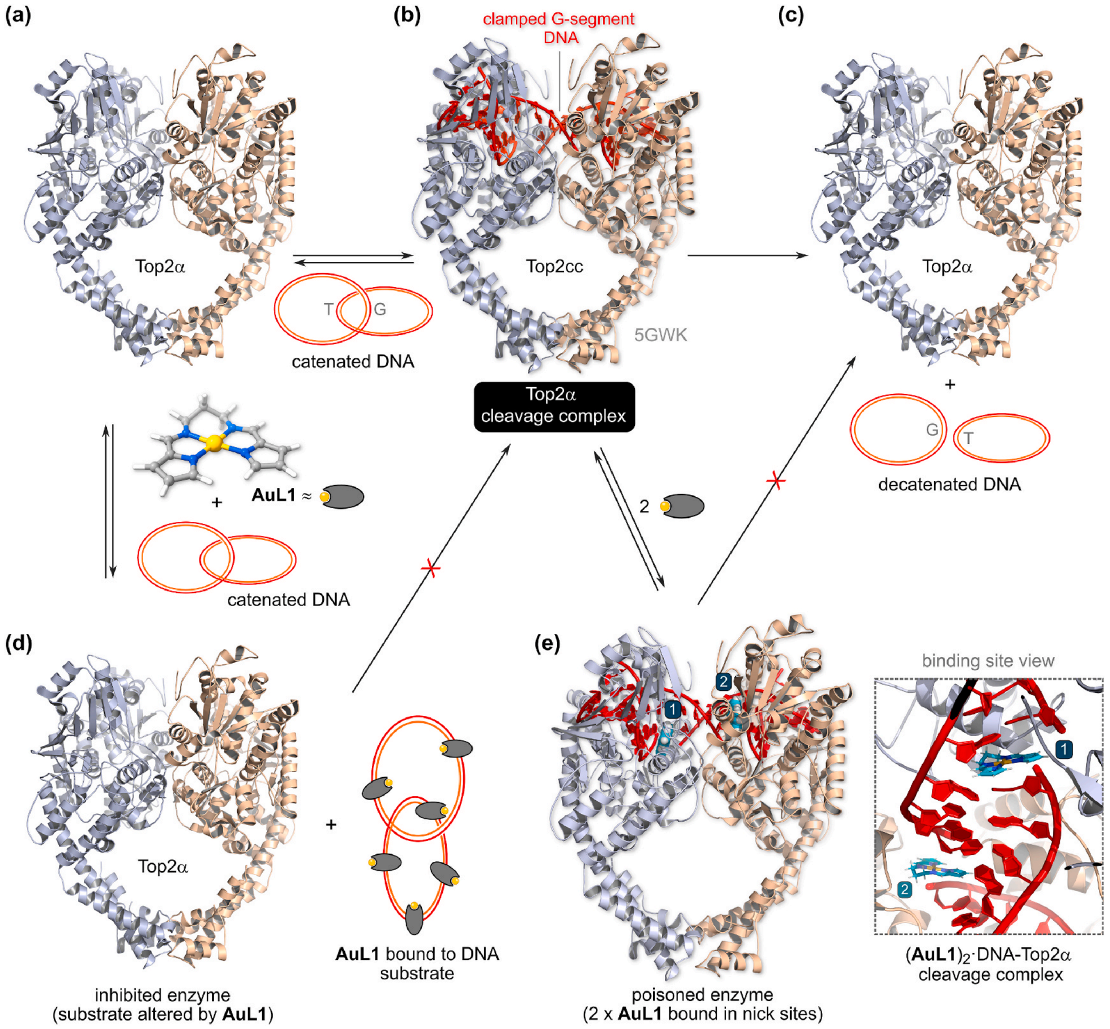

Fig. 6. Illustration of critical events in the catalytic cycle of human Top IIα (hereafter Top II) under normal conditions (no inhibitor) and with **AuL1**. (a) Catenated DNA is bound by Top II, which uses Mg^{2+}-catalyzed hydrolysis to introduce a double-strand break 4 bases apart in the sugar-phosphate backbone of the clamped G segment DNA. This state is the covalent cleavage complex (Top II cc) depicted in (b) and involves covalent phosphodiester bond linkages to the enzyme's two catalytic Tyr residues. In an ATP-dependent step, the Top II cc then parts the doubly nicked G segment DNA and facilitates transport (strand passage) of the T-segment DNA through the transient break. The enzyme then reseals the DNA nick sites, releases the decatenated DNA, and returns to its resting state in (c). In the presence of a DNA-binding catalytic inhibitor compound (CIC) like **AuL1**, the enzyme is blocked from binding its DNA substrate as depicted in (d). In the presence of an interfacial poison (IFP), such as **AuL1** at lower concentrations, the Top II cc nick sites are targeted by the metal complex (e) and poison the enzyme by preventing it from effecting T segment DNA transport and G-segment DNA re-ligation. Accumulation of poisoned Top II cc induces apoptosis. Note that **AuL1** has a higher affinity for the DNA nick sites in Top II cc (e) compared with unbound DNA (d), as evidenced by the gel data of Fig. 5. The structure in (e) represents the results of a GLIDE *in silico* docking experiment for **AuL1** with 5GWK; poses (1) and (2) had standard precision docking scores of −6.67 and −4.23 kcal mol^{-1}, respectively.

As shown in Fig. 7b and c, the reduced binding affinity is evident as a decrease in the formation of cleaved plasmid (linear DNA) in the gel electrophoresis experiments. The ethidium bromide (EB) gel in Fig. 7b reveals that **Pd(PrPyrr)** is approximately 100-fold less active than **AuL1** (500 nM), with cleaved plasmid DNA only detectable at a concentration of 50 μM for the Pd(II) complex. These findings emphasize that the Au (III) ion, and its unique chemical properties, are essential for the efficacy of the gold(III) chelates synthesized in this study.

The results of the EB gel (Fig. 7c) indicate that the free ligand (H_2L1) does not exhibit any Top II inhibition or poisoning activity, even at ultra-high concentrations. These collective findings are highly encouraging, as they demonstrate that the gold(III) chelates successfully reach their cellular targets before being reduced by GSH. Furthermore, the results highlight the critical role of the Au(III) ion in the efficacy of gold(III) chelates as chemotherapeutic agents, both *in vivo* and *in vitro*. While the rigid square-planar structure of **Pd(PrPyrr)** is ideal for a DNA intercalator, its activity is significantly diminished in the absence of the electrophilic Au(III) ion and difference in molecular charge.

2.9. DNA binding by the gold(III) chelates

From the reactions of **AuL1** with Top II, the catalytic inhibition was evident for [**AuL1**] > 10 μM, which appears to reflect binding of the compound to the enzyme's DNA substrate (in a fashion similar to that of etoposide [64]). We employed UV–vis titrations with calf thymus DNA (ctDNA) and varying concentrations of all three gold(III) complexes to test this hypothesis and to further investigate the binding affinity of the gold(III) complexes with DNA. In these experiments, ctDNA was titrated with the test gold(III) chelates at 37 °C in KH_2PO_4 buffer. Fig. 8a shows that the metal-to-ligand charge transfer (MLCT) band of the chelates was monitored at 382 nm, where changes in the absorbance indicates DNA binding (**AuL1** to ctDNA); equivalent plots for **AuL2** and **AuL3** are shown in Fig. S42). The maximum binding ratios of [ctDNA]:[**AuL1**], [ctDNA]:[**AuL3**], and [ctDNA]:[**AuL3**] were 11.6:1, 11.6:1, and 17.5:1, respectively, suggesting a higher DNA affinity for **AuL3**.

From Fig. 8a (and Fig. S42), the characteristic MLCT band at 382 nm and the π-π* band at 289 nm exhibit a decrease in absorbance intensity

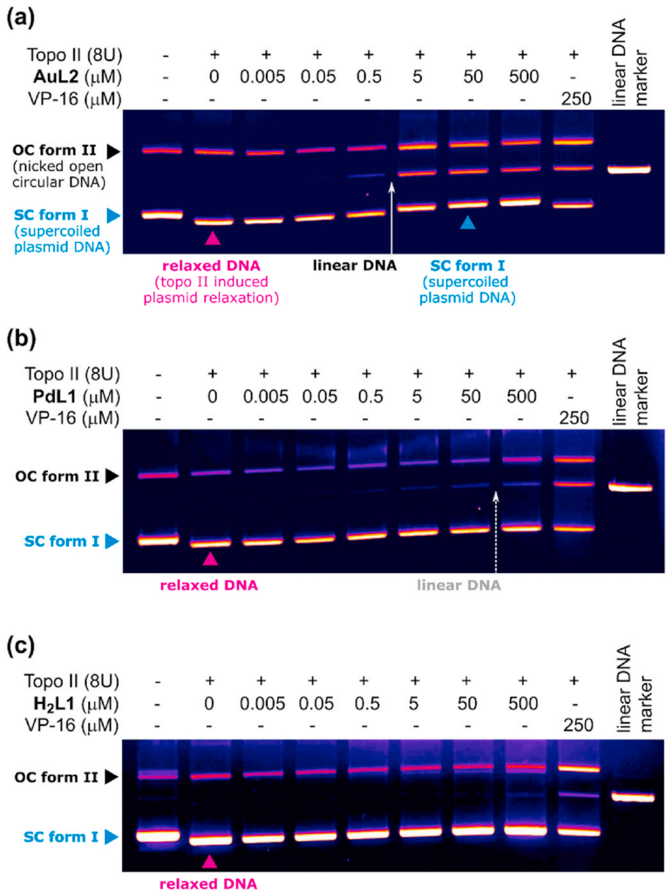

Fig. 7. Electrophoretic analysis (1 % agarose gel, 0.5 µg mL^{-1}, EB) of a topoisomerase II (Top II) DNA relaxation assay employing plasmid DNA (negatively supercoiled pHOT1 plasmid DNA; TopoGEN, Inc., 30 ng well^{-1}) as the substrate, an enzyme concentration of 8 units (U), etoposide (VP-16) as the Top II poison control (250 µM), and compounds (a) **AuL2**, (b) **Pd(PrPyrr)** and (c) **H_2L1** as the test agents over a concentration range of 0.005–500 µM. All annotated lanes, unless otherwise indicated, contain Top II.

ranging from 55.6 % ± 0.30 (**AuL1**) to 51.4 % ± 0.38 (**AuL3**), accompanied by a red shift from 382 nm to 394 nm. This bathochromic shift indicates that the gold(III) chelates are likely bound within a more polar environment, consistent with DNA binding. The decrease in absorbance at 382 nm during titration with ctDNA was fitted using the Hill model [72], yielding an R^2 value of 0.99 (Fig. 8a insert; Figs. S42b and d). From three independent experiments, the mean binding constants (K_a) at 310 K were calculated as 1.95 (±0.095) × 10^4 M^{-1}, 1.45 (±0.13) × 10^4 M^{-1}, and 2.66 (±0.1) × 10^4 M^{-1} for **AuL1**, **AuL2**, and **AuL3**, respectively (Table 3).

Typically, K_a values for groove binders range from 10^5 to 10^8 M^{-1} [73,74], which are higher than those observed for intercalators. We compared the binding constants of **AuL1**–**AuL3** to other gold(III) complexes known to interact with ctDNA (Fig. S43). Gold(III) macrocyclic complexes (4a) exhibit K_a values between 1.20 × 10^6 M^{-1} and 4.91 × 10^6 M^{-1}, while pseudo macrocyclic complexes show even higher affinities (2.85 × 10^6 M^{-1} to 6.61 × 10^6 M^{-1}) [67]. In contrast, CNC–Au(III) complexes (4b and 4c) have K_a values of 4.5 × 10^5 M^{-1} and 5.4 × 10^5 M^{-1} [75,76], respectively. Lastly, a carbazolide Au(III) complex (4d) has a K_a of 3.7 × 10^4 M^{-1} [77]. The K_a values for **AuL1**–**AuL3** are on the lower end of the range reported for DNA intercalators, suggesting a weaker binding affinity, potentially due to less favourable π-π stacking interactions or steric effects from the chelate ligands.

2.10. Linear and circular dichroism of DNA

With all DNA-binding compounds, the question arises as to whether the compound is an intercalator or a groove binder. The gold standard to answer this question is by using linear dichroism (UV-LD). The method incorporates the use of sheared DNA with increasing concentration of a test complex (**AuL1**–**AuL3**; Fig. 8b–and S46). All the gold(III) complexes are achiral, so they do not generate an inherent LD or CD signal. However, upon forming stable complexes with dsDNA (in this case, ctDNA), an induced dichroic spectrum is observed. This induced signal indicates the interaction of the chelates with DNA. Specifically, if the drug functions as a minor groove binder, it produces a positive dichroic signal. Conversely, intercalation results in a negative dichroic signal within the chromophoric region of the complexes (MLCT band for the gold(III) chelates) or in the near-UV π–π^* region (Fig. S45) [79].

All LD experiments were performed in KH_2PO_4 buffer (50 mM, pH 7.5), with ctDNA and varying [gold(III) chelate]/[DNA] ratios. The LD spectrum of ctDNA shows a strong negative signal at 260 nm, attributed to the nucleotides (purine and pyrimidine base pairs) [80]. Upon the addition of each gold(III) chelate, a concentration-dependent increase in the amplitude of the 260 nm minimum was observed (Fig. 8b and S46). This increase suggests enhanced DNA rigidity, indicating lengthening and stiffening of the double-helical DNA, consistent with intercalation and subsequent unwinding of the DNA strands (Fig. 8b) [81–83]. An induced dichroic signal appears between 350 and 430 nm, peaking at 394 nm, a region where the DNA base pairs do not absorb, indicating this signal originates solely from the chromophoric gold(III) chelates. Given that the gold(III) chelates are isotropic and cannot orient themselves in the flow field, the signal at 394 nm suggests an induced LD response, confirming that the chelates form a molecular complex with ctDNA and are intercalators.

CD spectroscopy was employed to observe conformational changes in ctDNA upon interaction with the Au(III) chelates (Fig. 8c and S47). Native B-form DNA exhibits four major transition bands at 210 nm, 220 nm, 244 nm, and 277 nm, which are characteristic of its double-helical conformation [84,85]. The maximum band at 277 nm reflects base stacking interactions, while the minima at 210 nm, 220 nm, and 244 nm indicate helicity of the DNA [84,86]. When the gold(III) chelates were added to the B-form DNA, the intensities of the 210 nm and 244 nm peaks decreased, while the intensity of the 277 nm peak increased. At a molar ratio of r = 2, the 277 nm band for **AuL1** and **AuL2** (Fig. 8c and S47a) showed distortion, suggesting DNA condensation induced by these chelates. This aggregation effect does not imply a conversion from B-form DNA to A-form DNA (which exhibits a maximum at 263 nm), but rather an ICD signal at 386 nm, indicating binding of the gold(III) chelates to ctDNA [87].

2.11. Molecular docking and molecular dynamics simulations

Theoretical ligand docking studies were employed using Glide XP to determine the binding mode of **AuL1** to an oligonucleotide DNA sequence. The two DNA X-ray structures used were; PDB: 425D (2.80 Å), which favours groove binding [88] and PDB: 4E1U (0.92 Å), which favours intercalation [78], for flexible ligand docking. This was used as an approximation theoretical method to corroborate our experimental data (Fig. 8a–c) and allow us to visualize how a ligand may bind to and interact with DNA. The key parameter elucidated from ligand docking is the docking score. It should be noted that these values typically do not correlate quantitatively with experimental binding or thermodynamic data (K_a or ΔG values) [89,90]. This is because ligand docking does not try to emulate a physical reaction between the incoming ligand and macromolecule. Hence, only qualitative comparisons can be made from docking scores. In our case, we wanted to determine if the Glide XP docking scores corroborated our experimental data which shows that **AuL1** is a DNA intercalator.

Glide XP docking of the gold(III) chelates to oligonucleotide DNA

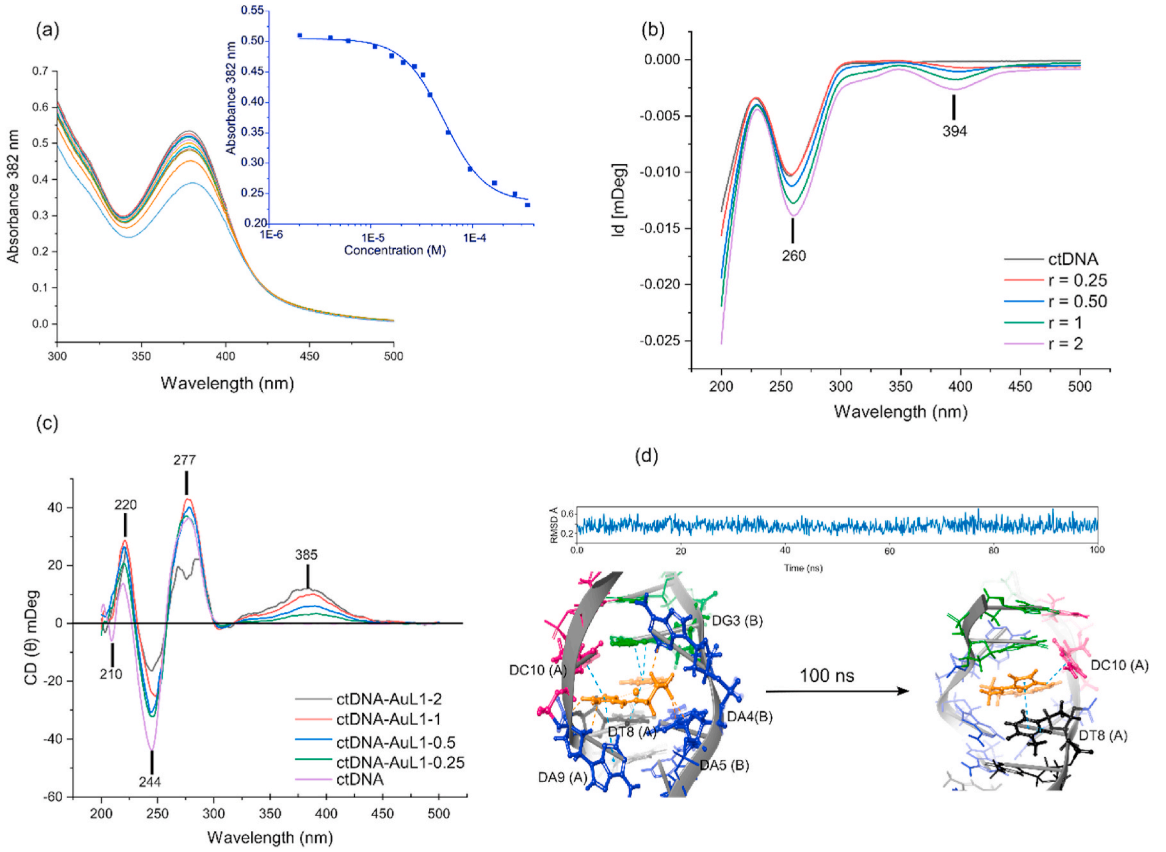

Fig. 8. (a) The UV–vis absorption spectra of **AuL1** and the insert represent the change in the absorbance at 382 nm of **AuL1** as a function of [ctDNA] fitted to the Hill model. The UV–visible absorption spectra of **AuL2** and **AuL3** are provided in the ESI. All reactions were carried out in KH_2PO_4 and after sequential additions of ctDNA (final [ctDNA] = 342 μM bp for **AuL1** and **AuL2** and 542 μM for **AuL3**). The Hill fits were used to calculate the dissociation constants and stoichiometric ratios of the Au(III) chelates binding to ctDNA. (b) The LD spectrum of **AuL1** with 100 μM of ctDNA at increasing [Au(III) chelate]:[ctDNA] ratios (*r*) of 0.25–2 in KH_2PO_4 (50 mM, pH 7.5) at 37 °C. The intense minimum at 260 nm represents ctDNA, and the 394 nm band represents an induced Au(III) chelate LD spectrum. (c) The CD spectrum of **AuL1** with 100 μM of ctDNA at increasing [Au(III) chelate]:[ctDNA] ratios (*r*) of 0.25–2 in KH_2PO_4 (50 mM, pH 7.5) at 37 °C. The intense maxima and minima from 210 to 277 nm represent ctDNA, and the 385 nm band represents an induced Au(III) chelate CD spectrum. (d) Molecular dynamic simulation (MD) over 100 ns of the best docked GLIDE XP structure of **AuL1** binding to an oligonucleotide of DNA (PDB 4E1U; 5′-D(CGGAAATTACCG)-3′) that is known to bind the cationic ruthenium complex $[Ru(bpy)_2(dppz)]^{2+}$ [78]. A large target grid was generated for ligand docking at the $[Ru(bpy)_2(dppz)]^{2+}$ site close to the centre of the DNA (with $[Ru(bpy)_2(dppz)]^{2+}$ removed), spanning 40 x 40 × 40 Å^3, thereby facilitating a search of alternative binding pockets radiating throughout the oligonucleotide. The RMSD indicates that there is minimal fluctuation of complex **AuL1** throughout the MD run. Docked poses of **AuL1** in the top-scoring site at 1ns and 100 ns are shown. Nucleic acid bases are colour coded: adenosine (blue), thymine (black), cytosine (pink), and guanosine (green). (For interpretation of the references to colour in this figure legend, the reader is referred to the Web version of this article.)

Table 3
Summary of the affinity constant of **AuL1**, **AuL2** and **AuL3** to ctDNA and GLIDE XP docking scores and selected interaction energy parameters for DNA targets prepared from ligand-free structures derived from PDB codes 425D and 4E1U. The docking runs were truncated to report only the top-scoring ligand pose for each ligand.

	ctDNA[a] × 10^4 M^{-1}	PDB:4E1U[b]			PDB: 425D[c]		
		Binding site residues	ΔG_{dock} kcal mol^{-1}	Glide energy kcal mol^{-1}	Binding site residues	ΔG_{dock} kcal mol^{-1}	Glide energy kcal mol^{-1}
AuL1	1.95 ± 0.095	AT	−4.594	−31.661	AT	−3.857	−31.418
AuL2	1.45 ± 0.13	AT	−4.947	−29.565	AT	−4.501	−35.686
AuL3	2.60 ± 0.10	AT	−4.437	−33.202	AT	−3.888	−34.919

[a] Experimental K_a delineated from the binding of **AuL1**–**AuL3** to ctDNA. PDB codes.
[b] 425D (biased towards groove binding).
[c] 4E1U (biased towards intercalating). The docking runs were truncated to report only the top-scoring ligand pose for each ligand. SD was omitted due to three independent docking experiments resulted in exact docking scores.

revealed that the complexes have a preference for PDB 4E1U (intercalative binding; Table 3), giving more favourable ΔG_{dock} scores compared with those to PDB 425D. The lowest best docked score (ΔG_{dock}) was in fact higher than the highest ΔG_{dock} score from PDB: 425D. The result corroborates the experimental data (*vide supra*), which indicates that all three gold(III) chelates bind to DNA via intercalation. Furthermore, the Glide XP best docked pose data indicate that all three complexes bind and intercalate DNA at the central 5′-AT-3′ step of the oligonucleotide (Fig. S48), though with a relatively low Glide docking score (ΔG_{bind} = −4.437 to −4.947 kcal mol^{-1}). As expected, the AT cluster sites are the preferred binding locations because they have been shown to exhibit the lowest binding energy [67]. Significantly, the Glide docking corroborated the experimentally observed K_a data order, wherein **AuL2** > **AuL1** > **AuL3**.

Following ligand docking of the gold(III) complexes to the DNA oligonucleotide (PDB: 4E1U), a 100 ns molecular dynamics (MD) simulation (Fig. 8d) was conducted on **AuL1** to assess the stability of the best Glide XP docked pose. MD simulations provide valuable insights into the interactions between macromolecules and ligands over time, capturing the system's dynamic behaviour and offering a more accurate reflection of physiological conditions. As shown in Fig. 8d, the root-mean-square deviation (RMSD) of **AuL1** remains relatively stable throughout the simulation trajectory (deviating between 0.2 and 0.6 Å). The deviations were minor, and therefore, the trajectory from 1 ns to 100 ns is only illustrated.

At the start of the trajectory, **AuL1** has π-π stacking and electrostatic interactions with DC10 (A), DA9 (A), DT8 (A), DG3 (B), DA5 (B) and DA4 (B) within the binding pocket. At 100 ns, and with some deviation, it is observed that **AuL1** remains closely interacting only with DC10 (A) and DT8 (A). Between 1 ns and 90 ns the minimal deviations in the RMSD are attributed to **AuL1** re-orientating into the DNA strand that has now being partly unwound due to intercalation from the complex. This insertion of **AuL1** into the oligonucleotide strand's base pairs results in the displacement of the π-stacked bases and initiates DNA uncoiling [91]. At the end of the 100 ns simulation, the DNA structure undergoes significant unwinding, disrupting the electrostatic interaction between **AuL1** and the nucleotides (Fig. 8d). The MD simulation data are consistent with the experimental UV-LD data shown in Fig. 8b, where the increase in the 260 nm minimum amplitude indicates ctDNA unwinding in response to increasing **AuL1** concentration. It should be noted that due to the limitations of the Maestro Suite (2022–4), DNA-specific RMSD and root-mean-square fluctuation (RMSF) values could not be calculated, requiring reliance on the trajectory output to infer ligand binding.

2.12. Importance of binding to HSA

The interaction of potential pharmaceutical compounds (**AuL1**–**AuL3** in this study) with plasma proteins is crucial in determining their bioavailability [92]. When evaluating potential therapeutic agents, thoroughly examining plasma protein binding becomes imperative. The interaction of the compounds with HSA, a crucial serum transport protein in the circulatory system, holds significant importance. This was highlighted by Rabbani et al. [93], who used a plethora of spectroscopic techniques and kinetic measurements to demonstrate that the binding interactions between the ligand and HSA are responsible for the ligand's distribution volume, metabolism, half-life, and ultimately its elimination rate. HSA has the capability to bind to a wide range of both naturally occurring metabolic compounds and externally administered therapeutic pharmaceuticals [94]. This binding interaction plays a pivotal role in altering the concentration of free drug, consequently affecting its availability and activity within the body [95]. HSA serves a dual role: it can serve as a reservoir for therapeutic agents, facilitating accessibility at concentrations beyond their plasma solubility, or it can expedite their clearance, potentially hindering their therapeutic efficacy. These effects can be deduced from the compound's affinity for binding to the protein [96–98]. When a drug demonstrates strong binding affinity to HSA, it causes a decrease in free drug concentrations, consequently prolonging the drug's half-life, as the bound fraction is less vulnerable to hepatic metabolic processes [96]. Therefore, examining the interaction between a potential drug and HSA stands as a vital first phase in understanding the compound's pharmacokinetics and pharmacodynamics, providing valuable insights into its potential therapeutic effectiveness [99]. In this study, we investigated several biophysical parameters for the binding of the present gold(III) chelates to HSA using isothermal titration calorimetry (ITC) and CD spectroscopy.

2.13. Isothermal titration calorimetry (ITC)

Binding and thermodynamic parameters were analysed using isothermal titration calorimetry (ITC), which provides quantitative data to elucidate the major forces driving small molecule-protein interactions [74-76] In this study, ITC quantified the heat exchange during the binding of **AuL1**–**AuL3** to HSA, complementing the steady-state fluorescence findings.

The raw heat released during binding of **AuL1**, **AuL2**, and **AuL3** to HSA is presented in Fig. 9 and S50, along with integrated heat data fitted to a one-site isothermal binding model. The thermograms illustrate heat release over time, with each injection producing a peak representing the maximum heat released or absorbed. The signal then returned to baseline, with subsequent peaks showing progressively lower heat release, indicating saturation of HSA's binding sites by the Au(III) chelates. Below each thermogram, the raw data is transformed into a binding curve [100,101]. The binding curve was fitted to a specific single-site binding model, and both K_a and ΔH were determined. The following equations calculated all other thermodynamic parameters:

$$\Delta G = \Delta G^\circ + RT\ln Q \tag{1}$$

$$\Delta G = -RT\ln K_a \tag{2}$$

$$\Delta G = \Delta H - T\Delta S \tag{3}$$

Where Q is the reaction quotient. ΔG° can be calculated from eq. (1), ΔG from eq. (2) and ΔS from eq. (3). A summary of the binding and thermodynamic parameters is reported in Table 3.

The binding constant (K_a) values, 6.83×10^4 M^{-1} (±0.03) for **AuL1**, 1.2×10^5 M^{-1} (±0.01) for **AuL2,** and 8.25×10^4 M^{-1} (±0.004) for **AuL3**, indicate moderate affinity of the gold(III) chelates for HSA. These results suggest that the metallodrugs are unlikely to be extensively retained by serum proteins *in vivo*. The K_a values are comparable to those reported for chiral Schiff base congeners [61]. The binding affinity of metal complexes to HSA depends on both the metal centre and the organic ligand. In previous studies, **H_2L1**–**H_2L3** were metalated with Pt (II) ions [102,103], and while the same trend was observed with the bridging alkyl group OH > H_2 > CH_3, the K_a values differed, reflecting the distinct interactions mediated by the metal ions.

The thermodynamic parameters (ΔH, $-T\Delta S$ and ΔG) delineated from ITC thermograms of **AuL1**, **AuL2**, and **AuL3** with HSA in KH_2PO_4 buffer (50 mM, pH 7.5) are reported in Table 4. All three reactions are

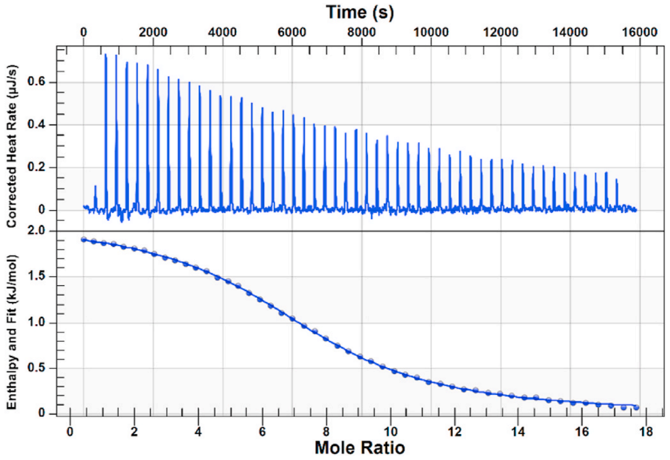

Fig. 9. Binding thermodynamics for **AuL1** interacting with HSA (20 μM, in 50 mM KH_2PO_4, pH 7.5) measured by ITC. The top panel represents the raw heat released by each injection. The bottom panel indicates the integrated heat corresponding to each injection. The solid line shows the best-fitting isothermal binding model. Experiments were performed at 298 K. The data for **AuL2** and **AuL3** are presented in Fig. S50.

Table 4
Summary of the thermodynamic parameters obtained by ITC for **AuL1**, **AuL2**, and **AuL3** binding to HSA.

	K_a (× 10^5 M^{-1})	ΔG (kJ·mol^{-1})	ΔH (kJ·mol^{-1})	$-T\Delta S$ (kJ·mol^{-1})
AuL1	0.683 (0.03)	−27.50 (0.1)	52.5 (2.12)	−79.9 (2.9)
AuL2	1.20 (0.01)	−28.60 (0.1)	47.3 (1.1)	−75.9 (3)
AuL3	0.825 (0.004)	−28.07 (0.02)	24.0 (1.8)	−52.2 (2)

exergonic [104] with ΔG ranging from −27.5 kJ mol^{-1} for **AuL1** to −28.6 kJ mol^{-1} for **AuL2** at 298 K. This is visually depicted in Fig. 10a, where the ΔG values fall in a narrow range for the three gold(III) chelates. The similarity of the ΔG values strongly suggest a consistent binding mode for the complexes to HSA, indicating enthalpy/entropy compensation. The energy difference is minimal and can be attributed to the binding of the three gold(III) chelates in a similar position within the protein in a 1:1 stoichiometric ratio.

By applying the Gibbs-Helmholtz relationship (Eq. (3)) and analyzing the experimental data (Table 4), the influence of the ligand structure for **AuL1**–**AuL3** on the thermodynamic parameters governing ligand uptake by HSA was evaluated (Fig. 10). In Fig. 10b, $T\Delta S/\ \Delta G$ is plotted against $\Delta H/\Delta G$ where it is clear the data fit the linear relationship. All three chelates fall in the bottom-left quadrant, where $\Delta H > 0$ and $\Delta S > 0$, which is consistent with entropic control of the binding process. For the gold(III) chelates, spontaneity is ensured as changes in $\Delta H/\Delta G$ are compensated by corresponding changes in $T\Delta S/\ \Delta G$. The ratios $T\Delta S/\Delta G$ and $\Delta H/\Delta G$ for the Au(III) chelates increase together in the order **AuL1** < **AuL2** < **AuL3**.

The trend suggests that the thermodynamics for the uptake of **AuL1**–**AuL3** by HSA are mainly influenced by the ligand's bridging alkyl chain since all three Au(III) chelates share the same cationic metal centre. The binding of **AuL1** and **AuL3** to HSA is evidently dominated by interactions with the cationic Au(III) centre and π–π interactions, favoured by their planar structures. In contrast, the hydroxyl group of **AuL2** facilitates additional interactions with the protein and solvent by hydrogen-bonding, enhancing its binding affinity, thereby edging the reaction towards the Gibbs-Helmholtz quadrant for both enthalpy and entropy-driven reactions [105].

The reactions between HSA and the Au(III) chelates are significantly endothermic, with ΔH values ranging from 24.0 kJ mol^{-1} for **AuL3** to 52.5 kJ mol^{-1} for **AuL1**. Fig. 10b emphasizes the dominance of the entropy term, indicating that the binding process is entropically driven. This conclusion is further supported by the thermograms in Fig. 9 and S50. Differences in the alkyl linking chains within the gold(III) chelates are highlighted in their markedly different ΔH and ΔS values. Specifically, **AuL1** requires more energy for binding, as indicated by its higher ΔH, which is offset by its correspondingly higher ΔS values. The ΔS values, listed in Table 4, decrease in the order **AuL1** > **AuL2** > **AuL3**, ranging from 268 J K^{-1} mol^{-1} (**AuL1**) to 175 J K^{-1} mol^{-1} (**AuL3**). This trend suggests that the more hydrophilic Au(III) chelates induce significant desolvation of ordered water molecules at Sudlow's site I within HSA upon binding.

In summary, binding of the three Au(III) chelates to HSA is entropically driven, with positive ΔH and ΔS values. The primary binding forces involve hydrophobic interactions [106,107]. The positive ΔH can be attributed to two factors: (i) the partial disruption of the hydrophobic cavity in subdomain IIA by the gold(III) chelates, and (ii) destruction of the "iceberg" water structure surrounding the gold(III) chelates upon their entry into subdomain IIA [108].

2.14. Far-UV CD spectroscopy

The secondary structure of proteins can be easily determined using far-UV CD spectroscopy, which takes advantage of several spectral regions, including peptide bonds, aromatic amino acids side chains, and disulphide bonds [109]. HSA is predominantly an α-helix protein, with α-helices constituting 67 % of its structure [110]. In Fig. 11a, we employed far-UV CD spectroscopy (186–260 nm) to delineate the impact of the Au(III) chelates on the secondary structure of the protein.

The far-UV CD spectrum of native HSA displayed the characteristic double minima at 208 ± 1 nm and 222 ± 1 nm, consistent with a dominantly α-helix rich protein [111]. The bands at 208, 222, and 193 nm are assigned to π–π*, n–π*, and π–π* transitions, respectively [112,113]. All three transitions involve the amide groups of the peptide backbone [109,111]. From Fig. 11a, uptake of the Au(III) chelates by HSA negligibly impacts the secondary structure of the protein, despite the moderately high affinity of the complexes for HSA (Table 4). The CD spectrum of HSA undergoes dose-dependent changes, with the bands at 208 ± 1 and 222 ± 1 nm approaching zero, indicating alterations in the secondary structure of HSA. The maximum at 193 nm decreased with increasing concentrations of **AuL2** and **AuL3** but remained essentially unchanged for **AuL1** (Fig. 11a and S51).

To quantify the changes in the secondary structure of HSA, we further analysed the spectra using JASCO Spectra Manager™ [114]. This allowed us to calculate the percentage composition of α-helical coils, turns, and unordered coils present for each HSA···Au(III) complex (Table S12). The dominant secondary structure domains were α-helices

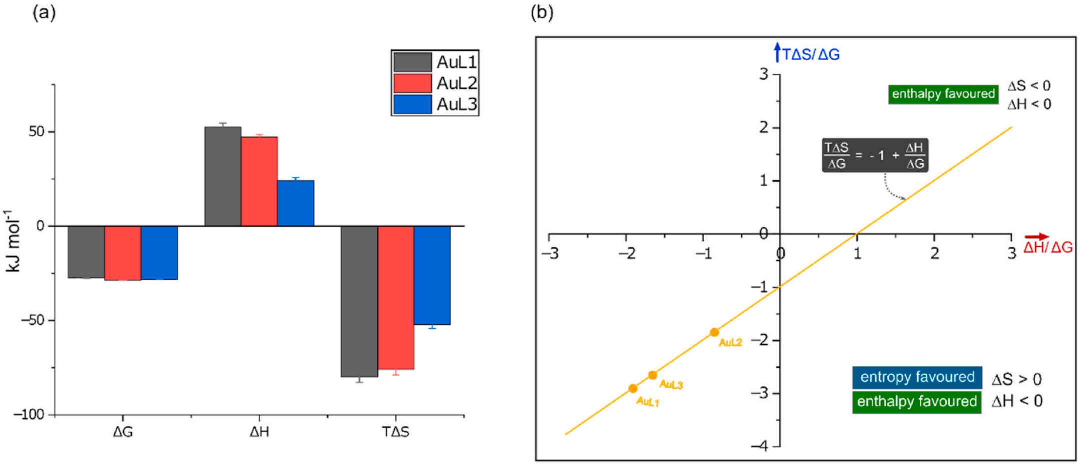

Fig. 10. (a) Comparison of the thermodynamic parameters (298 K) governing the reactions of the three gold(III) chelates with HSA. (b) Plot of the Gibbs-Helmholtz relationship (eq. (3)) for the reaction of the three complexes with HSA at 298 K in 50 mM KH_2PO_4 buffer at pH 7.50. The straight line fit of the data gives $R^2 = 0.9993$ with a slope and intercept of 1. The plot highlights how the identity of the bis (pyrrolide-imine) Schiff base chelate influences the reaction thermodynamics. For all reactions, $\Delta G < 0$. (For interpretation of the references to colour in this figure legend, the reader is referred to the Web version of this article.)

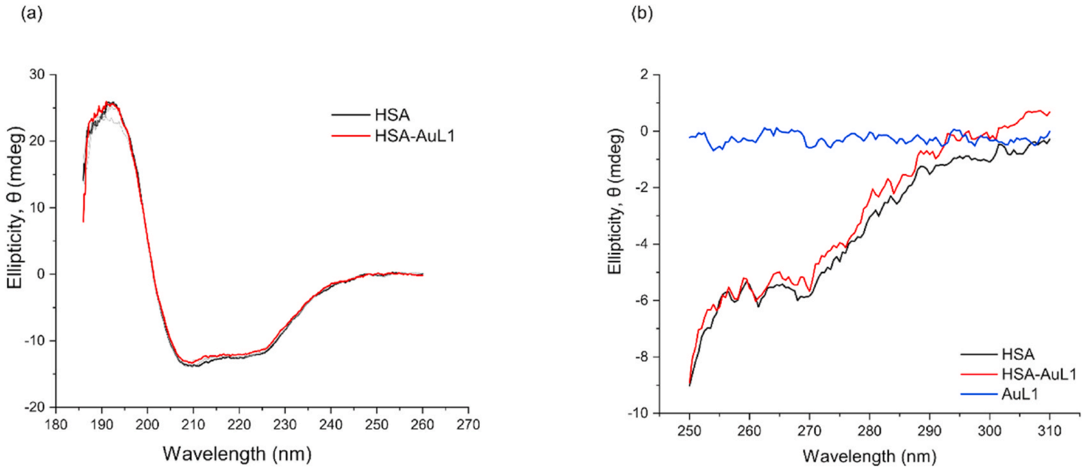

Fig. 11. (a) Plots of the far-UV CD spectra of native HSA and the protein incubated with saturating doses of **AuL1** recorded at 298 K in 50 mM KH_2PO_4 buffer at pH 7.5 The concentration of the Au(III) chelate ranged from 0 to 6 μM, the native protein is represented by the black line, and the Au(III) chelate–HSA adduct at 6 μM is represented by the black line. The grey lines represents the Au(III) chelate at 0.3, 1.5, and 3 μM. (b) Plots of the near-UV CD spectra of native HSA and the protein incubated with a 1:1 ratio of **AuL1** were recorded at 298 K in 50 mM KH_2PO_4 buffer at pH 7.50. The data represents unsmoothed spectra in the fine structure region for the protein. Perturbations in the protein structure around Phe (250–270 nm), Tyr (~280 nm), and Trp (285–300 nm) residues are evident.

(~58 %) and unordered coils (~31 %). The α-helicity of HSA was ~58 %, but it was diminished in the presence of each gold(III) chelate within a range of 3.72 % (**AuL1**) to 7.83 % (**AuL2**). The decrease in α-helicity was accompanied by an increase in random turns and β-sheets. Interestingly, the solution-state secondary structure composition of HSA differs from that of native HSA in the solid state [49] (68.5 % α-helix, 0 % β-sheet, 9.6 % turns, and 21.9 % unordered coils; PDB code 1BM0, analysed with BeStSel [115]). However, our solution phase far-UV CD data are consistent with solution state spectral decompositions reported previously [116–118]. Overall, it is accepted that enhanced subdomain mobility and general thermal motion/disorder accounts for the decrease of α-helicity seen in the solid state [111,119].

2.15. Near-UV CD spectroscopy

To elucidate the conformational changes induced by **AuL1**–**AuL3** to the tertiary structure of HSA, we employed near-UV CD spectroscopy in the range of 250–310 nm (Fig. 11b and S52). A typical near-UV–CD spectrum is dominated by fine structure signals from the aromatic amino acid residues and tend to reflect the local symmetry of the chromophore, notably Trp (285–300 nm), Tyr (275–285 nm), and Phe (250–270 nm) [120]. Significant transition peaks for HSA were observed, including two minima at 262 and 280 nm and a maximum at 290 nm, which are attributed to the presence of disulfide bonds and the aromatic amino acids [121].

The near-UV CD spectra of HSA (Fig. 11b and S52) in the absence of **AuL1** exhibited a broadened peak at 290 nm, accompanied by fine structure features between 290 and 305 nm attributed to the Trp-214 residue. Additionally, between 275 and 285 nm, there was a peak at 284 nm with a shoulder at 287 nm, likely originating from the 18 Tyr residues within HSA. The Phe fingerprint region, spanning 255–270 nm, displayed a peak near 257 nm. The presence of two minima at 262 and 268 nm, along with a shoulder at 279 nm, are characteristics of disulfide bonds [109,122,123], of which HSA possesses 17 [110]. Phe, Tyr, and Trp all have π–π* transitions (^1L_a and ^1L_b) and can participate in π bonding, which is crucial for ligand binding, as discussed earlier. Therefore, perturbations in the fine structure of the protein can indicate conformational changes within the protein itself or alterations in the environment surrounding the aromatic amino acids [124].

The three gold(III) chelates induced changes to the near-UV CD spectra, indicating their binding to the protein in close enough proximity to affect the fine structure surrounding the aromatic amino acid residues. **AuL1** and **AuL3** showed a redshift of 2 nm at 290 nm, **AuL2** caused the 290 nm band to split and blue shift by ~1 nm. There were no significant shifts in the disulfide bond fingerprint region, suggesting minimal changes to the bonds. Overall, the binding of gold(III) chelates to HSA was shown to induce slight conformational changes in both the secondary (Fig. 11a and S51) and tertiary structures (Fig. 11b and S52) of the protein. These conformational changes in the tertiary structure may account for the enthalpy differences observed in our ITC data [125].

Studying the structural changes of HSA in the presence of the Au(III) chelates is important for the overall study. This has direct impact on the (i) binding specificity, since structural changes can alter the shape and polarity of binding pockets, affecting how specific drugs interact with HSA. (ii) Allosteric effects: Conformational changes at one site can impact other binding sites, influencing drug binding cooperativity or competition. (iii) Drug efficacy and distribution: Variations in HSA structure can modify how drugs are distributed, metabolized, and eliminated, ultimately impacting their therapeutic efficacy and pharmacokinetics [18,94].

3. Conclusion

The three cationic bis(pyrrolide-imine) Au(III) Schiff base chelates **AuL1**, **AuL2** and **AuL3** studied here displayed unique mean growth percentages of 78 %, 98 % and 92 %, respectively, in an NCI-60 1-dose screen against 60 human cancer cell lines. A subsequent five-dose NCI-60 screen for **AuL1** and **AuL3** afforded mean GI_{50} values of 7.3 μM, 11.5 μM and IC_{50} values of 15 and 31 μM, respectively, commensurate with significant cytotoxicity. Hierarchical cluster analysis of the NCI-60 data for **AuL1** and **AuL3** indicated a direct correlation of the NCI-60 cytotoxicity profile for the Au(III) complexes with etoposide, a potent Top II poison. Our statistical data reflecting targeting of Top II by **AuL1** signals a novel mechanism of action for this class of compounds and warranted a further mechanistic study. Agarose gel Top II inhibition assays indicated that **AuL1** is a dual mode inhibitor of Top II. At low doses (0.5–50 μM), **AuL1** is an interfacial poison of the enzyme (IFP, $K_{a1} = 7.46 \times 10^{-6}\ M^{-1}$), while between 50 and 500 μM **AuL1** blocks enzyme-DNA binding, thereby operating as an unconventional catalytic inhibitor compound (CIC) for Top II. **AuL2** exhibited a similar dual-mode Top II inhibition profile to **AuL1**, but was insufficiently active in the NCI-60 live cell cytotoxicity assay possibly due to involvement of the ligand's hydroxyl group in mediating metabolic degradation or clearance via an efflux pump. Since DNA is the main substrate for Top II, we investigated the binding of **AuL1**–**AuL3** to ctDNA. Linear dichroism data suggested all three chelates bound to ctDNA via intercalation with modest affinity constants (K_a) of $1.95\ (\pm 0.095) \times 10^4$, $1.45\ (\pm 0.13) \times 10^4$ and $2.66 \pm (0.1) \times 10^4\ \mathrm{M}^{-1}$ for **AuL1**, **AuL2** and **AuL3**, respectively, at 310 K (Table 2). The interaction of **AuL1** and **AuL2** with human serum albumin (HSA) was subsequently investigated by ITC to understand how the alkyl chain bridge within the ligand impacts uptake of the cationic complexes by the protein. The HSA affinity constants, K_a, followed the order: **AuL2** > **AuL1** > **AuL3**, with a stoichiometric ratio ~1:1 (ligand: protein). The gold(III) chelates bind to HSA with positive ΔH and ΔS values, and negative ΔG values, reflecting a spontaneous entropically-driven process governed by hydrophobic and electrostatic interactions. $T\Delta S/\Delta G$ and $\Delta H/\Delta G$ increase together in the order: **AuL1** > **AuL3** > **AuL2**. All three chelates preferentially bound to Sudlow's site I (shown through molecular docking). Finally, far- and near-UV CD data indicated that the Au(III) chelates minimally perturb the protein's secondary and tertiary structure.

CRediT authorship contribution statement

Sheldon Sookai: Writing – review & editing, Writing – original draft, Visualization, Validation, Resources, Methodology, Investigation, Formal analysis, Data curation, Conceptualization. **Matthew Akerman:** Methodology, Investigation, Data curation. **Mia Færch:** Formal analysis, Data curation. **Yasien Sayed:** Writing – review & editing, Supervision. **Orde Q. Munro:** Writing – review & editing, Visualization, Validation, Supervision, Resources, Funding acquisition, Formal analysis, Data curation, Conceptualization.

Declaration of competing interest

All five authors have no competing interests and collectively state that we have nothing to declare.

Acknowledgements

This work is based on research supported by the South African Research Chairs Initiative of the Department of Science and Innovation (DSI) and National Research Foundation (NRF) of South Africa (Grant No 64799, OQM). The authors thank WITS University and the NRF for funding to purchase a JASCO J-1500 MCD spectrometer (Grant No 116177, OQM) and a dual-wavelength Bruker D8 Venture X-ray diffractometer (Grant No 129920, OQM). We also thank the Centre for High Performance Computing (Project CHEM1633, CHPC, Cape Town) for both the CPU time and resources needed for the DFT simulations and Desmond MD simulations. The authors would also like to thank Manuel Fernandes for his expertise in small molecule crystallography. The authors thank the National Cancer Institute Developmental Therapeutics Program (NCI-DTP, USA) for screening **AuL1, AuL2** and **AuL3**.

Appendix A. Supplementary data

Supplementary data to this article can be found online at https://doi.org/10.1016/j.ejmech.2025.117330.

Data availability

Data will be made available on request.

References

[1] B. Rosenberg, L. Van Camp, T. Krigas, Inhibition of cell division in Escherichia coli by electrolysis products from a platinum electrode, Nature 205 (1965) 698–699, https://doi.org/10.1038/205698a0.

[2] S.E. Sherman, D. Gibson, A.H.-J. Wang, S.J. Lippard, X-ray structure of the major adduct of the anticancer drug cisplatin with DNA: *cis* -$[\mathrm{Pt(NH_3)_2}\ \{\mathrm{d(pGpG)}\}]$, Science 230 (1985) 412–417, https://doi.org/10.1126/science.4048939.

[3] M. Coll, S.E. Sherman, D. Gibson, S.J. Lippard, A.H.-J. Wang, Molecular structure of the complex formed between the anticancer drug cisplatin and d(pGpG): $C222_1$ crystal form, J. Biomol. Struct. Dyn. 8 (1990) 315–330, https://doi.org/10.1080/07391102.1990.10507808.

[4] C.J. Ziegler, A.P. Silverman, S.J. Lippard, High-throughput Synthesis and screening of platinum drug candidates, JBIC, J. Biol. Inorg. Chem. 5 (2000) 774–783.

[5] S. Alassadi, J. Pisani, M, J. Wheate, N. A, Chemical perspective on the clinical use of platinum-based anticancer drugs, Dalton Trans. 51 (2022) 10835–10846, https://doi.org/10.1039/D2DT01875F.

[6] M.J. Hannon, Metal-based anticancer drugs: from a past anchored in platinum chemistry to a post-genomic future of diverse chemistry and biology, Pure Appl. Chem. 79 (2007) 2243–2261.

[7] J.H. Schiller, D. Harrington, C.P. Belani, C. Langer, A. Sandler, J. Krook, J. Zhu, D.H. Johnson, Eastern cooperative oncology group comparison of four chemotherapy regimens for advanced non-small-cell lung cancer, N. Engl. J. Med. 346 (2002) 92–98, https://doi.org/10.1056/NEJMoa011954.

[8] K.S. Lovejoy, S.J. Lippard, Non-traditional platinum compounds for improved accumulation, oral bioavailability, and tumor targeting, Dalton Trans. (2009) 10651–10659.

[9] L. Kelland, The resurgence of platinum-based cancer chemotherapy, Nat. Rev. Cancer 7 (2007) 573–584, https://doi.org/10.1038/nrc2167.

[10] K.D. Mjos, C. Orvig, Metallodrugs in medicinal inorganic chemistry, Chem. Rev. 114 (2014) 4540–4563, https://doi.org/10.1021/cr400460s.

[11] Z. Guo, P.J. Sadler, Metals in medicine, Angew. Chem. Int. Ed. 38 (1999) 1512–1531, https://doi.org/10.1002/(SICI)1521-3773(19990601)38:11<1512::AID-ANIE1512>3.0. CO;2-Y.

[12] K.O. Alfarouk, C.-M. Stock, S. Taylor, M. Walsh, A.K. Muddathir, D. Verduzco, A. H.H. Bashir, O.Y. Mohammed, G.O. Elhassan, S. Harguindey, et al., Resistance to cancer chemotherapy: failure in drug response from ADME to P-gp, Cancer Cell Int. 15 (2015) 71, https://doi.org/10.1186/s12935-015-0221-1.

[13] S.-H. Chen, J.-Y. Chang, New insights into mechanisms of cisplatin resistance: from tumor cell to microenvironment, Int. J. Mol. Sci. 20 (2019) 4136, https://doi.org/10.3390/ijms20174136.

[14] R. Oun, E. Moussa, Y, J. Wheate, N. The side effects of platinum-based chemotherapy drugs: a review for chemists, Dalton Trans. 47 (2018) 6645–6653, https://doi.org/10.1039/C8DT00838H.

[15] I. Kostova, Gold coordination complexes as anticancer agents, Anti Cancer Agents Med. Chem. 6 (2006) 19–32, https://doi.org/10.2174/187152006774755500.

[16] A. Casini, C. Hartinger, C. Gabbiani, E. Mini, P.J. Dyson, B.K. Keppler, L. Messori, Gold(III) compounds as anticancer agents: relevance of gold-protein interactions for their mechanism of action, J. Inorg. Biochem. 102 (2008) 564–575, https://doi.org/10.1016/j.jinorgbio.2007.11.003.

[17] A. Casini, L. Messori, Molecular mechanisms and proposed targets for selected anticancer gold compounds, Curr. Top. Med. Chem. 11 (2011) 2647–2660, https://doi.org/10.2174/156802611798040732.

[18] C. Gabbiani, A. Casini, L. Messori, A. Guerri, M.A. Cinellu, G. Minghetti, M. Corsini, C. Rosani, P. Zanello, M. Arca, Structural characterization, solution studies, and DFT calculations on a series of binuclear gold(III) oxo complexes: relationships to biological properties, Inorg. Chem. 47 (2008) 2368–2379, https://doi.org/10.1021/ic701254s.

[19] D. Van der Westhuizen, C.A. Slabber, M.A. Fernandes, D.F. Joubert, G. Kleinhans, C.J. van der Westhuizen, A. Stander, O.Q. Munro, D.I. Bezuidenhout, A cytotoxic bis (1, 2, 3-triazol-5-ylidene) carbazolide gold (III) complex targets DNA by partial intercalation, Chem. Eur J. 27 (2021) 8295–8307.

[20] V. Milacic, D. Chen, L. Ronconi, K.R. Landis-Piwowar, D. Fregona, Q.P. Dou, A novel anticancer gold (III) dithiocarbamate compound inhibits the activity of a purified 20S proteasome and 26S proteasome in human breast cancer cell cultures and xenografts, Cancer Res. 66 (2006) 10478–10486.

[21] R. D. Teo, H. B. Gray, P. Lim, J. Termini, E. Domeshek, Z. Gross, A cytotoxic and cytostatic gold(iii) corrole, Chem. Commun. 50 (2014) 13789–13792, https://doi.org/10.1039/C4CC06577H.

[22] B. Bertrand, J. Fernandez-Cestau, J. Angulo, M.M.D. Cominetti, Z.A.E. Waller, M. Searcey, M.A. O'Connell, M. Bochmann, Cytotoxicity of pyrazine-based cyclometalated (CˆNpzˆC)Au(III) carbene complexes: impact of the nature of the ancillary ligand on the biological properties, Inorg. Chem. 56 (2017) 5728–5740, https://doi.org/10.1021/acs.inorgchem.7b00339.

[23] C.-M. Che, R.W.-Y. Sun, W.-Y. Yu, C.-B. Ko, N. Zhu, H. Sun, Gold (III) porphyrins as a new class of anticancer drugs: cytotoxicity, DNA binding and induction of apoptosis in human cervix epitheloid cancer cells, Chem. Commun. (2003) 1718–1719.

[24] K.J. Akerman, A.M. Fagenson, V. Cyril, M. Taylor, M.T. Muller, M.P. Akerman, O. Q. Munro, Gold(III) macrocycles: nucleotide-specific unconventional catalytic inhibitors of human topoisomerase I, J. Am. Chem. Soc. 136 (2014) 5670–5682, https://doi.org/10.1021/ja412350f.

[25] L. Messori, F. Abbate, G. Marcon, P. Orioli, M. Fontani, E. Mini, T. Mazzei, S. Carotti, T. O'Connell, P. Zanello, Gold(III) complexes as potential antitumor agents: solution chemistry and cytotoxic properties of some selected gold(III) compounds, J. Med. Chem. 43 (2000) 3541–3548, https://doi.org/10.1021/jm990492u.

[26] V. Bhardwaj, D. Gumber, V. Abbot, S. Dhiman, P. Pyrrole Sharma, A resourceful small molecule in key medicinal hetero-aromatics, RSC Adv. 5 (2015) 15233–15266.

[27] R.N. Brogden, R.C. Heel, T.M. Speight, G.S. Avery, Tolmetin: a review of its pharmacological properties and therapeutic efficacy in rheumatic diseases, Drugs 15 (1978) 429–450, https://doi.org/10.2165/00003495-197815060-00002.

[28] H.D. Langtry, J.A. Balfour, Glimepiride, Drugs 55 (1998) 563–584, https://doi.org/10.2165/00003495-199855040-00007.

[29] M. Atkins, C.A. Jones, P. Kirkpatrick, Sunitinib maleate, Nat. Rev. Drug Discov. 5 (2006) 279–280, https://doi.org/10.1038/nrd2012.

[30] S. Hannah, V.M. Lynch, N. Gerasimchuk, D. Magda, J.L. Sessler, Synthesis of a metal-free texaphyrin, Org. Lett. 3 (2001) 3911–3914, https://doi.org/10.1021/ol016757s.

[31] J.L. Sessler, T.D. Mody, G.W. Hemmi, V. Lynch, Synthesis and structural characterization of lanthanide(III) texaphyrins, Inorg. Chem. 32 (1993) 3175–3187, https://doi.org/10.1021/ic00066a032.

[32] H. Patel, R. Mick, J. Finlay, T.C. Zhu, E. Rickter, K.A. Cengel, S.B. Malkowicz, S. M. Hahn, T.M. Busch, Motexafin lutetium-photodynamic therapy of prostate cancer: short-and long-term effects on prostate-specific antigen, Clin. Cancer Res. 14 (2008) 4869–4876.

[33] J.L. Nitiss, Targeting DNA topoisomerase II in cancer chemotherapy, Nat. Rev. Cancer 9 (2009) 338–350.

[34] J.V. Walker, J.L. Nitiss, DNA topoisomerase II as a target for cancer chemotherapy, Cancer Invest. 20 (2002) 570–589.

[35] S.H. Chen, N.-L. Chan, T. Hsieh, New mechanistic and functional insights into DNA topoisomerases, Annu. Rev. Biochem. 82 (2013) 139–170.

[36] J.E. Deweese, N. Osheroff, Coordinating the two protomer active sites of human topoisomerase IIα: nicks as topoisomerase II poisons, Biochemistry 48 (2009) 1439–1441.

[37] T. Stuchinskaya, L.A. Mitchenall, A.J. Schoeffler, K.D. Corbett, J.M. Berger, A. D. Bates, A. Maxwell, How do type II topoisomerases use ATP hydrolysis to simplify DNA topology beyond equilibrium? Investigating the relaxation reaction of nonsupercoiling type II topoisomerases, J. Mol. Biol. 385 (2009) 1397–1408.

[38] Y. Pommier, E. Leo, H. Zhang, C. Marchand, DNA topoisomerases and their poisoning by anticancer and antibacterial drugs, Chem. Biol. 17 (2010) 421–433, https://doi.org/10.1016/j.chembiol.2010.04.012.

[39] J.E. Deweese, N. Osheroff, The DNA cleavage reaction of topoisomerase II: wolf in sheep's clothing, Nucleic Acids Res. 37 (2009) 738–748, https://doi.org/10.1093/nar/gkn937.

[40] J.L. Nitiss, DNA topoisomerase II and its growing repertoire of biological functions, Nat. Rev. Cancer 9 (2009) 327–337.

[41] S.M. Vos, E.M. Tretter, B.H. Schmidt, J.M. Berger, All tangled up: how cells direct, manage and exploit topoisomerase function, Nat. Rev. Mol. Cell Biol. 12 (2011) 827–841.

[42] Y. Pommier, Drugging topoisomerases: lessons and challenges, ACS Chem. Biol. 8 (2013) 82–95.

[43] Y. Pommier, C. Marchand, Interfacial inhibitors: targeting macromolecular complexes, Nat. Rev. Drug Discov. 11 (2012) 25–36.

[44] C.-C. Wu, Y.-C. Li, Y.-R. Wang, T.-K. Li, N.-L. Chan, On the structural basis and design guidelines for type II topoisomerase-targeting anticancer drugs, Nucleic Acids Res. 41 (2013) 10630–10640.

[45] C.-C. Wu, T.-K. Li, L. Farh, L.-Y. Lin, T.-S. Lin, Y.-J. Yu, T.-J. Yen, C.-W. Chiang, N.-L. Chan, Structural basis of type II topoisomerase inhibition by the anticancer drug etoposide, Science 333 (2011) 459–462, https://doi.org/10.1126/science.1204117.

[46] M.P. Akerman, O.Q. Munro, M. Mongane, J.A. van Staden, W.I.D. Rae, C. J. Bester, B. Marjanovic-Painter, Z. Szucs, J.R. Zeevaart, Biodistribution (as determined by the radiolabelled equivalent) of a gold(III) bis(pyrrolide-imine) Schiff base complex: a potential chemotherapeutic, J. Label. Compd. Radiopharm. 56 (2013) 530–535, https://doi.org/10.1002/jlcr.3068.

[47] S. Curry, Lessons from the crystallographic analysis of small molecule binding to human serum albumin, Drug Metabol. Pharmacokinet. 24 (2009) 342–357.

[48] G.J. Quinlan, G.S. Martin, T.W. Evans, Albumin: biochemical properties and therapeutic potential, Hepatology 41 (2005) 1211–1219, https://doi.org/10.1002/hep.20720.

[49] X.M. He, D.C. Carter, Atomic structure and chemistry of human serum albumin, Nature 358 (1992) 209–215, https://doi.org/10.1038/358209a0.

[50] P.A. Zunszain, J. Ghuman, T. Komatsu, E. Tsuchida, S. Curry, Crystal structural analysis of human serum albumin complexed with hemin and fatty acid, BMC Struct. Biol. 3 (2003) 6, https://doi.org/10.1186/1472-6807-3-6.

[51] G. Rabbani, S.N. Ahn, Structure, enzymatic activities, glycation and therapeutic potential of human serum albumin: a natural cargo, Int. J. Biol. Macromol. 123 (2019) 979–990, https://doi.org/10.1016/j.ijbiomac.2018.11.053.

[52] G. Sudlow, D.J. Birkett, D.N. Wade, Further characterization of specific drug binding sites on human serum albumin, Mol. Pharmacol. 12 (1976) 1052–1061.

[53] G. Sudlow, D.J. Birkett, D.N. Wade, The characterization of two specific drug binding sites on human serum albumin, Mol. Pharmacol. 11 (1975) 824–832.

[54] O.Q. Munro, K.J. Akerman, P. Akerman, Gold Complexes for Use in the Treatment of Cancer, 2016.

[55] K. Hüttinger, C. Förster, T. Bund, D. Hinderberger, K. Heinze, Stereochemical consequences of oxygen atom transfer and electron transfer in imido/oxido molybdenum(IV, V, VI) complexes with two unsymmetric bidentate ligands, Inorg. Chem. 51 (2012) 4180–4192, https://doi.org/10.1021/ic202588u.

[56] J. Ghuman, P.A. Zunszain, I. Petitpas, A.A. Bhattacharya, M. Otagiri, S. Curry, Structural basis of the drug-binding specificity of human serum albumin, J. Mol. Biol. 353 (2005) 38–52, https://doi.org/10.1016/j.jmb.2005.07.075.

[57] K.J. Akerman, A.M. Fagenson, V. Cyril, M. Taylor, M.T. Muller, M.P. Akerman, O. Q. Munro, Gold(III) macrocycles: nucleotide-specific unconventional catalytic inhibitors of human topoisomerase I, J. Am. Chem. Soc. 136 (2014) 5670–5682, https://doi.org/10.1021/ja412350f.

[58] C. Ct, D.F. Shriver, P.W. Atkins, C.H. Langford, Inorganic Chemistry, Oxford University Press, vol. 50, BACHELOR Sci. Chem. Sess. 20172018 124 Credits 1 Univ. COURSES 20 Credits Course Code Course Name Credit, 1996, p. 7. CT1-3 References: 1.

[59] E. Alessio, Thirty years of the drug candidate NAMI-A and the myths in the field of ruthenium anticancer compounds: a personal perspective, Eur. J. Inorg. Chem. 2017 (2017) 1549–1560, https://doi.org/10.1002/ejic.201600986.

[60] D. van der Westhuizen, D.I. Bezuidenhout, O.Q. Munro, Cancer Molecular biology and strategies for the design of cytotoxic gold(i) and gold(iii) complexes: a tutorial review, Dalton Trans. 50 (2021) 17413–17437, https://doi.org/10.1039/D1DT02783B.

[61] S. Sookai, M.P. Akerman, O.Q. Munro, Chiral Au(iii) chelates exhibit unique NCI-60 cytotoxicity profiles and interactions with human serum albumin, Dalton Trans. 53 (2024) 5089–5104, https://doi.org/10.1039/D3DT04024K.

[62] T. Inada, A. Ichikawa, T. Kubota, Y. Ogata, A.R. Moossa, R.M. Hoffman, 5-FU-Induced apoptosis correlates with efficacy against human gastric and colon cancer xenografts in nude mice, Anticancer Res. 17 (1997) 1965–1971.

[63] H. Takeda, M. Haisa, Y. Naomoto, R. Kawashima, K. Satomoto, T. Yamatuji, N. Tanaka, Effect of 5-fluorouracil on cell cycle regulatory proteins in human colon cancer cell line, Jpn. J. Cancer Res. 90 (1999) 677–684.

[64] G.M. Cragg, D.G. Kingston, D.J. Newman, Anticancer Agents from Natural Products, CRC press, 2005.

[65] A. Eastman, The mechanism of action of cisplatin: from adducts to apoptosis, in: B. Lippert (Ed.), Cisplatin: Chemistry and Biochemistry of a Leading Anticancer Drug, Wiley, 1999, pp. 111–134. ISBN 978-3-906390-20-8.

[66] C.R. Wilson, A.M. Fagenson, W. Ruangpradit, M.T. Muller, O.Q. Munro, Gold (III) complexes of pyridyl-and isoquinolylamido ligands: structural, spectroscopic, and biological studies of a new class of dual topoisomerase I and II inhibitors, Inorg. Chem. 52 (2013) 7889–7906.

[67] K.J. Akerman, A.M. Fagenson, V. Cyril, M. Taylor, M.T. Muller, M.P. Akerman, O. Q. Munro, Gold(III) macrocycles: nucleotide-specific unconventional catalytic inhibitors of human topoisomerase I, J. Am. Chem. Soc. 136 (2014) 5670–5682, https://doi.org/10.1021/ja412350f.

[68] K.C. Dong, J.M. Berger, Structural basis for gate-DNA recognition and bending by type IIA topoisomerases, Nature 450 (2007) 1201–1205.

[69] K.M. Tewey, T.C. Rowe, L. Yang, B.D. Halligan, L.-F. Liu, Adriamycin-induced DNA damage mediated by mammalian DNA topoisomerase II, Science 226 (1984) 466–468.

[70] G. Capranico, F. Zunino, K.W. Kohn, Y. Pommier, Sequence-selective topoisomerase II inhibition by anthracycline derivatives in SV40 DNA: relationship with DNA binding affinity and cytotoxicity, Biochemistry 29 (1990) 562–569.

[71] I.G. Darvey, What factors are responsible for the greater yield of ATP per carbon atom when fatty acids are completely oxidised to CO2 and water compared with glucose? Biochem. Educ. 27 (1999) 209–210.

[72] S. Goutelle, M. Maurin, F. Rougier, X. Barbaut, L. Bourguignon, M. Ducher, P. Maire, The Hill equation: a review of its capabilities in pharmacological modelling, Fundam. Clin. Pharmacol. 22 (2008) 633–648.

[73] B.H. Geierstanger, D.E. Wemmer, Complexes of the minor groove of DNA, Annu. Rev. Biophys. Biomol. Struct. 24 (1995) 463–493.

[74] P.E. Pjura, K. Grzeskowiak, R.E. Dickerson, Binding of hoechst 33258 to the minor groove of B-DNA, J. Mol. Biol. 197 (1987) 257–271.

[75] C.K. Li, R.W. Sun, S.C. Kui, N. Zhu, C. Che, Anticancer cyclometalated [AuIIIm (C∧ N∧ C) mL] N+ compounds: Synthesis and cytotoxic properties, Chem. Eur J. 12 (2006) 5253–5266.

[76] J.J. Yan, A.L.-F. Chow, C.-H. Leung, R.W.-Y. Sun, D.-L. Ma, C.-M. Che, Cyclometalated gold (III) complexes with N-heterocyclic carbene ligands as topoisomerase I poisons, Chem. Commun. 46 (2010) 3893–3895.

[77] D. Van der Westhuizen, C.A. Slabber, M.A. Fernandes, D.F. Joubert, G. Kleinhans, C.J. van der Westhuizen, A. Stander, O.Q. Munro, D.I. Bezuidenhout, A cytotoxic bis (1, 2, 3-triazol-5-ylidene) carbazolide gold (III) complex targets DNA by partial intercalation, Chem. Eur J. 27 (2021) 8295–8307.

[78] H. Song, J.T. Kaiser, J.K. Barton, Crystal structure of Δ-[Ru (bpy) 2 dppz] 2+ bound to mismatched DNA reveals side-by-side metalloinsertion and intercalation, Nat. Chem. 4 (2012) 615–620.

[79] R. Lyng, T. Härd, B. Norden, Induced CD of DNA intercalators: electric dipole allowed transitions, Biopolym. Orig. Res. Biomol. 26 (1987) 1327–1345.

[80] B. Nordén, T. Kurucsev, Analysing DNA complexes by circular and linear dichroism, J. Mol. Recogn. 7 (1994) 141–155.

[81] Y. Kubota, K. Hashimoto, K. Fujita, M. Wakita, E. Miyanohana, Y. Fujisaki, Flow dichroism, flow polarized fluorescence and viscosity of the DNA · acridine complexes, Biochim. Biophys. Acta BBA - Nucleic Acids Protein Synth. 478 (1977) 23–32, https://doi.org/10.1016/0005-2787(77)90240-4.

[82] P.C. Dedon, Determination of binding mode: intercalation, Curr. Protoc. Nucleic Acid Chem. (00) (2000) 8.1.1–8.1.13, https://doi.org/10.1002/0471142700.nc0801s00.

[83] M.A. Galindo, D. Olea, M.A. Romero, J. Gómez, P. del Castillo, M.J. Hannon, A. Rodger, F. Zamora, J.A.R. Navarro, Design and non-covalent DNA binding of platinum(II) metallacalix[4]Arenes, Chem. Eur J. 13 (2007) 5075–5081, https://doi.org/10.1002/chem.200601581.

[84] M. Vorlícková, Conformational transitions of alternating purine-pyrimidine DNAs in perchlorate ethanol solutions, Biophys. J. 69 (1995) 2033–2043.

[85] J. Kypr, M. Vorlíčková, Circular dichroism spectroscopy reveals invariant conformation of guanine runs in DNA, Biopolym. Orig. Res. Biomol. 67 (2002) 275–277.

[86] M. Vorlícková, I. Kejnovská, J. Kovanda, J. Kypr, Conformational properties of DNA strands containing guanine-adenine and thymine-adenine repeats, Nucleic Acids Res. 26 (1998) 1509–1514.

[87] E. Froehlich, J.S. Mandeville, C.M. Weinert, L. Kreplak, H.A. Tajmir-Riahi, Bundling and aggregation of DNA by cationic dendrimers, Biomacromolecules 12 (2011) 511–517.

[88] H. Rozenberg, D. Rabinovich, F. Frolow, R.S. Hegde, Z. Shakked, Structural code for DNA recognition revealed in crystal structures of papillomavirus E2-DNA targets, Proc. Natl. Acad. Sci. 95 (1998) 15194–15199, https://doi.org/10.1073/pnas.95.26.15194.

[89] A.R. Leach, B.K. Shoichet, C.E. Peishoff, Prediction of Protein−Ligand interactions. Docking and scoring: successes and gaps, J. Med. Chem. 49 (2006) 5851–5855, https://doi.org/10.1021/jm060999m.

[90] G.L. Warren, C.W. Andrews, A.-M. Capelli, B. Clarke, J. LaLonde, M.H. Lambert, M. Lindvall, N. Nevins, S.F. Semus, S. Senger, et al., A critical assessment of docking programs and scoring functions, J. Med. Chem. 49 (2006) 5912–5931, https://doi.org/10.1021/jm050362n.

[91] M.P. O'Hagan, S. Haldar, J.C. Morales, A.J. Mulholland, M.C. Galan, Enhanced sampling molecular dynamics simulations correctly predict the diverse activities of a series of stiff-stilbene G-quadruplex DNA ligands, Chem. Sci. 12 (2021) 1415–1426.

[92] J. Costa Pessoa, I. Tomaz, Transport of therapeutic vanadium and ruthenium complexes by blood plasma components, Curr. Med. Chem. 17 (2010) 3701–3738.

[93] G. Rabbani, M.H. Baig, A.T. Jan, E. Ju Lee, M.V. Khan, M. Zaman, A.-E. Farouk, R. H. Khan, I. Choi, Binding of erucic acid with human serum albumin using a spectroscopic and molecular docking study, Int. J. Biol. Macromol. 105 (2017) 1572–1580, https://doi.org/10.1016/j.ijbiomac.2017.04.051.

[94] G. Rabbani, E.J. Lee, K. Ahmad, M.H. Baig, I. Choi, Binding of tolperisone hydrochloride with human serum albumin: effects on the conformation, thermodynamics, and activity of HSA, Mol. Pharm. 15 (2018) 1445–1456, https://doi.org/10.1021/acs.molpharmaceut.7b00976.

[95] G. Rabbani, S.N. Ahn, Roles of human serum albumin in prediction, diagnoses and treatment of COVID-19, Int. J. Biol. Macromol. 193 (2021) 948–955.

[96] T. Bohnert, L.-S. Gan, Plasma protein binding: from discovery to development, J. Pharmaceut. Sci. 102 (2013) 2953–2994.

[97] G. Colmenarejo, *In silico* prediction of drug-binding strengths to human serum albumin, Med. Res. Rev. 23 (2003) 275–301, https://doi.org/10.1002/med.10039.

[98] B. Demoro, R.F.M. de Almeida, F. Marques, C.P. Matos, L. Otero, J.C. Pessoa, I. Santos, A. Rodríguez, V. Moreno, J. Lorenzo, et al., Screening organometallic binuclear thiosemicarbazone ruthenium complexes as potential anti-tumour agents: cytotoxic activity and human serum albumin binding mechanism, Dalton Trans. 42 (2013) 7131–7146, https://doi.org/10.1039/C3DT00028A.

[99] G. Rabbani, S.N. Ahn, Structure, enzymatic activities, glycation and therapeutic potential of human serum albumin: a natural cargo, Int. J. Biol. Macromol. 123 (2019) 979–990, https://doi.org/10.1016/j.ijbiomac.2018.11.053.

[100] R. Perozzo, G. Folkers, L. Scapozza, Thermodynamics of protein–ligand interactions: history, presence, and future aspects, J. Recept. Signal Transduction 24 (2004) 1–52, https://doi.org/10.1081/RRS-120037896.

[101] J.B. Chaires, A thermodynamic signature for drug–DNA binding mode, Arch. Biochem. Biophys. 453 (2006) 26–31.

[102] S. Sookai, O.Q. Munro, Complexities of the interaction of NiII, PdII and PtII pyrrole-imine chelates with human serum albumin, ChemistryEurope 1 (2023) e202300012, https://doi.org/10.1002/ceur.202300012.

[103] S. Sookai, O.Q. Munro, Spectroscopic and computational study of the interaction of Pt(II) pyrrole-imine chelates with human serum albumin, Dalton Trans. (2023), https://doi.org/10.1039/D3DT02039H.

[104] P.D. Ross, S. Subramanian, Thermodynamics of protein association reactions: forces contributing to stability, Biochemistry 20 (1981) 3096–3102, https://doi.org/10.1021/bi00514a017.

[105] G. Rabbani, M.H. Baig, E.J. Lee, W.-K. Cho, J.Y. Ma, I. Choi, Biophysical study on the interaction between eperisone hydrochloride and human serum albumin using spectroscopic, calorimetric, and molecular docking analyses, Mol. Pharm. 14 (2017) 1656–1665, https://doi.org/10.1021/acs.molpharmaceut.6b01124.

[106] X. Du, Y. Li, Y.-L. Xia, S.-M. Ai, J. Liang, P. Sang, X.-L. Ji, S.-Q. Liu, Insights into protein–ligand interactions: mechanisms, models, and methods, Int. J. Mol. Sci. 17 (2016) 144, https://doi.org/10.3390/ijms17020144.

[107] P.D. Ross, S. Subramanian, Thermodynamics of protein association reactions: forces contributing to stability, Biochemistry 20 (1981) 3096–3102, https://doi.org/10.1021/bi00514a017.

[108] J. Grabowska, A. Kuffel, J. Zielkiewicz, Revealing the frank–evans "iceberg" structures within the solvation layer around hydrophobic solutes, J. Phys. Chem. B 125 (2021) 1611–1617, https://doi.org/10.1021/acs.jpcb.0c09489.

[109] S.M. Kelly, T.J. Jess, N.C. Price, How to study proteins by circular dichroism, Biochim. Biophys. Acta BBA - Proteins Proteomics 1751 (2005) 119–139, https://doi.org/10.1016/j.bbapap.2005.06.005.

[110] X.M. He, D.C. Carter, Atomic structure and chemistry of human serum albumin, Nature 358 (1992) 209–215, https://doi.org/10.1038/358209a0.

[111] N. Sreerama, R.W. Woody, Computation and analysis of protein circular dichroism spectra, in: Methods in Enzymology; Numerical Computer Methods, Part D, vol. 383, Academic Press, 2004, pp. 318–351.

[112] G. Rabbani, J. Kaur, E. Ahmad, R.H. Khan, S.K. Jain, Structural characteristics of thermostable immunogenic outer membrane protein from Salmonella enterica serovar typhi, Appl. Microbiol. Biotechnol. 98 (2014) 2533–2543, https://doi.org/10.1007/s00253-013-5123-3.

[113] G. Rabbani, E. Ahmad, M.V. Khan, M.T. Ashraf, R. Bhat, R.H. Khan, Impact of structural stability of cold adapted Candida Antarctica lipase B (CaLB): in relation to pH, chemical and thermal denaturation, RSC Adv. 5 (2015) 20115–20131, https://doi.org/10.1039/C4RA17093H.

[114] Z.S. do Monte, C.S. Ramos, Development and validation of a method for the analysis of paroxetine HCl by circular dichroism, Chirality 25 (2013) 211–214, https://doi.org/10.1002/chir.22122.

[115] A. Micsonai, F. Wien, É. Bulyáki, J. Kun, É. Moussong, Y.-H. Lee, Y. Goto, M. Réfrégiers, J. BeStSel Kardos, A web server for accurate protein secondary structure prediction and fold recognition from the circular dichroism spectra, Nucleic Acids Res. 46 (2018) W315–W322, https://doi.org/10.1093/nar/gky497.

[116] F. Mohammadi, A.-K. Bordbar, A. Divsalar, K. Mohammadi, A.A. Saboury, Analysis of binding interaction of curcumin and diacetylcurcumin with human and bovine serum albumin using fluorescence and circular dichroism spectroscopy, Protein J. 28 (2009) 189–196, https://doi.org/10.1007/s10930-009-9184-1.

[117] H.A. Tajmir-Riahi, C.N. N'soukpoé-Kossi, D. Joly, Structural analysis of protein–DNA and protein–RNA interactions by FTIR, UV-visible and CD spectroscopic methods, Spectroscopy 23 (2009) 81–101, https://doi.org/10.3233/SPE-2009-0371.

[118] O. Duman, S. Tunç, B. Kancı Bozoğlan, Characterization of the binding of metoprolol tartrate and guaifenesin drugs to human serum albumin and human hemoglobin proteins by fluorescence and circular dichroism spectroscopy, J. Fluoresc. 23 (2013) 659–669, https://doi.org/10.1007/s10895-013-1177-y.

[119] P. Alam, S.K. Chaturvedi, T. Anwar, M.K. Siddiqi, M.R. Ajmal, G. Badr, M. H. Mahmoud, R. Hasan Khan, Biophysical and molecular docking insight into the interaction of cytosine β-D arabinofuranoside with human serum albumin, J. Lumin. 164 (2015) 123–130, https://doi.org/10.1016/j.jlumin.2015.03.011.

[120] G. Rabbani, E. Ahmad, N. Zaidi, S. Fatima, R.H. Khan, pH-induced molten globule state of rhizopus niveus lipase is more resistant against thermal and chemical denaturation than its native state, Cell Biochem. Biophys. 62 (2012) 487–499, https://doi.org/10.1007/s12013-011-9335-9.

[121] D. Lafitte, P.O. Tsvetkov, F. Devred, R. Toci, F. Barras, C. Briand, A.A. Makarov, J. Haiech, Cation binding mode of fully oxidised calmodulin explained by the unfolding of the apostate, Biochim. Biophys. Acta BBA-Proteins Proteomics 1600 (2002) 105–110.

[122] B. Ahmad, S. Parveen, R.H. Khan, Effect of albumin conformation on the binding of ciprofloxacin to human serum albumin: a novel approach directly assigning binding site, Biomacromolecules 7 (2006) 1350–1356, https://doi.org/10.1021/bm050996b.

[123] C. Sun, J. Yang, X. Wu, X. Huang, F. Wang, S. Liu, Unfolding and refolding of bovine serum albumin induced by cetylpyridinium bromide, Biophys. J. 88 (2005) 3518–3524, https://doi.org/10.1529/biophysj.104.051516.

[124] X.-X. Cheng, X.-Y. Fan, F.-L. Jiang, Y. Liu, K.-L. Lei, Resonance energy transfer, pH-induced folded states and the molecular interaction of human serum albumin and icariin, Luminescence 30 (2015) 1026–1033.

[125] N. Zaidi, M.R. Ajmal, G. Rabbani, E. Ahmad, R.H. Khan, A comprehensive insight into binding of hippuric acid to human serum albumin: a study to uncover its impaired elimination through hemodialysis, PLoS One 8 (2013) e71422, https://doi.org/10.1371/journal.pone.0071422.